

Journal of Geophysical Research: Earth Surface

RESEARCH ARTICLE

10.1029/2018JF004753

Key Points:

- Distinct timescales of bedload transport fluctuations through a boulder array are identified
- Key hydraulic mechanisms in the vicinity of boulders influence boulder controls on bed morphology and bedload transport
- Boulder relative submergence and Froude number describe the nature of the flow in the boulder vicinity and location of depositional patches

Supporting Information:

- Supporting Information S1
- Data Set S1

Correspondence to:

Thanos Papanicolaou,
tpapanic@utk.edu

Citation:

Papanicolaou, A. N. (T.), Tsakiris, A. G., Wyssmann, M. A., & Kramer, C. M. (2018). Boulder array effects on bedload pulses and depositional patches. *Journal of Geophysical Research: Earth Surface*, 123, 2925–2953. <https://doi.org/10.1029/2018JF004753>

Received 10 MAY 2018

Accepted 3 OCT 2018

Accepted article online 11 OCT 2018

Published online 14 NOV 2018

Boulder Array Effects on Bedload Pulses and Depositional Patches

A. N. (Thanos) Papanicolaou¹ , Achilleas G. Tsakiris^{1,2}, Micah A. Wyssmann¹ , and Casey M. Kramer²

¹Hydraulics and Sedimentation Laboratory (HSL), Department of Civil and Environmental Engineering, The University of Tennessee, Knoxville, TN, USA, ²Northwest Hydraulic Consultants, Olympia, WA, USA

Abstract The influence of boulders in high gradient gravel-bed rivers can be significant. Yet few studies have isolated their role in regulating bedload. It is hypothesized that boulder relative submergence and the corresponding eddies developing around boulders affect the frequency of bedload pulsations and the location of sediment deposits. Results show the occurrence of two distinct timescales in bedload exiting a boulder array, which were identified via time series analysis. These are the small-scale periodicity, P_S , and the large-scale periodicity, P_L . P_S was identified in the range of 4–6 min and is believed to result from congested bedload movement due to reduced conveyance area within the array. P_L was identified in the range of 8–46 min. It is suggested that P_L corresponds to large bedload releases around boulders, which the authors consider to be caused by feedbacks between boulder eddies and bedload deposits. It is also found that boulder submergence and Froude number, Fr , influence the location of predominant deposition. At High Relative Submergence, deposition occurs in the boulder wake regions. At Low Relative Submergence, deposition instead occurs upstream of boulders in locations that depend on Fr . For $Fr < 1$, material deposits in the stoss of boulders due to the necklace structure of the horseshoe vortex. However, for $Fr > 1$, material deposits at the flanks of boulders due to the influence of local wave crests around boulders. The trapping efficiency of boulders reduces the dimensionless mean bedload transport rate by three orders of magnitude compared to conditions without boulders.

1. Introduction

Improved understanding of bedload transport is of paramount importance in high gradient gravel-bed rivers, where the coarse material delivered to river reaches from adjacent hillslopes and tributary basins is predominantly transported as bedload. River beds in these streams are often characterized by large boulders that together with smaller mobile sediments create a bed surface that has a multimodal, poorly sorted grain size distribution (Bathurst, 1987; Lenzi et al., 2006; Rickenmann, 2001; Schneider et al., 2015; Yager et al., 2007, 2012). Boulders are often organized in arrays occupying about 1–20% of the bed plan view area (e.g., Byrd et al., 2000; Nitsche et al., 2011). Due to their prominent size, boulders often remain immobile and become entrainable only during rare flood events (Bathurst, 1987; Turowski et al., 2009).

During lower flows, which prevail throughout the majority of the year in high gradient systems, boulders often protrude through the water surface. This condition is referred to in the literature as Low Relative Submergence (LRS) and occurs when the ratio of the flow depth to the boulder or clast diameter, H/d_c , is less than one ($H/d_c < 1$). In contrast, during higher flow events driven by either snowmelt or rainfall (e.g., Pitlick, 1994) the High Relative Submergence (HRS) regime occurs when H/d_c is greater than three ($H/d_c > 3$; Bettess, 1984; Shamloo et al., 2001). There is also an intermediate submergence regime, that is, when $1 < H/d_c < 3$ (Nikora et al., 2001; Shamloo et al., 2001). For intermediate submergence conditions, however, the boulder influence on flow and bedload transport can vary with the level of submergence. As a first step, the focus of this research is on the examination of boulder effects on bedload under HRS and LRS conditions.

The influence of boulders in high gradient gravel-bed rivers where they are prevalent can be significant and multifaceted. Boulders have been documented to bear a portion of the total bed shear stress through form drag (Nitsche et al., 2011; Schneider et al., 2015; Yager et al., 2007), create spatial variability in bed shear stress (Dey et al., 2011; Monsalve et al., 2016; Papanicolaou et al., 2012; Shamloo et al., 2001), and generate turbulent eddy structures (Hardy et al., 2009; Papanicolaou & Tsakiris, 2017; Tsakiris, Papanicolaou, Hajimirzaie et al.,

2014). Through the modification of reach-scale hydrodynamics, boulders also induce bedload fluctuations by affecting the rate of particle entrainment and deposition in their vicinity (e.g., Heays et al., 2014). By regulating the deposition and mobilization of incoming material, boulders also alter bed surface structure or patchiness (Ghilardi et al., 2014a; Piton & Recking, 2015; Yager et al., 2007). Preliminary findings of Papanicolaou and Kramer (2005) also suggest that the location of depositional patches around boulders may be different depending on the level of submergence (i.e., HRS and LRS conditions) and surface wave characteristics around boulders.

While several studies have looked into the interplay of boulders with flow, few studies have examined the effects of boulders on bedload fluctuations. The potential linkage of boulders with bedload fluctuations has been recently investigated in the experiments conducted by Ghilardi et al. (2014a, 2014b), where boulders were placed atop beds of natural, mobile gravel sediment to closely mimic natural settings in high gradient gravel-bed rivers. These studies showed that boulders promoted cycles of sediment deposition and mobilization around them, which affected bedload fluctuation timescales. The cycles were manifested first, through deposition of the incoming particles, thereby leading to gradual and eventually complete boulder burial; and, second, through subsequent bed mobilization in the absence of boulder hiding effects. Ghilardi et al. (2014a) implicitly connected this cyclical phase of sediment deposition and mobilization around boulders with the observed bedload rate pulsations and suggested that boulders affected the timescale of transported bedload. While the Ghilardi et al. (2014a, 2014b) studies have certainly provided unique insights into the dynamic interactions of boulders with flow hydraulics and reach-scale bed morphology, their studies did not isolate the direct influences that boulders may have on bedload rate fluctuations. In the Ghilardi et al. (2014a, 2014b) experiments, multiple interrelated processes occurred, such as vertical sorting and the development and breakdown of armor layers, which could have contributed to bedload fluctuations observed during their experiments, in addition to the fluctuations promoted by the boulders alone. Therefore, it is reasonable to suggest that the contributions of vertical sorting and armor layer to bedload during their experiments may have camouflaged the explicit role that boulders play on bedload fluctuations.

The overarching goal of this study is to isolate the role of boulders on mean bedload transport and pulsations under different submergence conditions. To accomplish this goal, this study develops a laboratory experimental setup that uses particles transported within an equispaced boulder array and aims to remove the influences of other complex processes on bedload fluctuations. In particular, the influence of bed irregularity is removed by using a well-packed bed of spherical particles and the influences of vertical sorting and bed armoring are removed since the bed was immobile and the mobile bedload was too large to infiltrate the bed.

In meeting this study's goal, the methodological design also takes advantage of previous knowledge about the frictional characteristics that an array of boulders can exert on flow (Papanicolaou et al., 2011, 2012) and the linkage that exists between boulders and local flow structure on bedload (Papanicolaou & Tsakiris, 2017). Last but not the least, the authors draw upon their experience gained in studying pulsation during bedload movement of sand-sized particles through a boulder array under LRS. Papanicolaou et al. (2011) showed that boulders modified bed morphological characteristics by promoting the development of depositional sand patches around individual boulders. Consecutive cycles of deposition and mobilization of sand were linked to pulses in the bedload fluxes, yet the Papanicolaou et al. (2011) study did not examine the timescale of these pulses or isolate the direct role that boulders play on bedload fluctuations.

Motivated by these findings, the present research builds on past research and examines the following supposition. The relative submergence of boulders and the corresponding eddies developing around them affect the magnitude and frequency of bedload pulsations and also the location of sediment deposits. We hypothesize that these effects are the outcome of the interactions between flow and boulders under different submergence conditions that affect eddies and water surface wave characteristics.

The specific objectives, pursued in this study, are to (1) identify the location and size of depositional patches in the vicinity of boulders under HRS and LRS conditions; (2) assess the effects of the boulder array on rates of exiting mean bedload transport and bedload trapping; and (3) discern the characteristic timescales in bedload rate fluctuations attributed to the boulder presence.

2. Methods

2.1. Experimental Methods and Design

As part of the methodology, attention was placed on the design of the laboratory experiments in order to isolate the effects that boulders have on bedload. The experiments were conducted using a tilting, water-recirculating flume that is 21.0 m long, 0.91 m wide, and 0.53 m deep. Glass spheres (sediment density, $\rho_s = 2545 \text{ kg/m}^3$) with median size $d_{50} = 19.1 \text{ mm}$ were utilized as mobile bedload. The mobile spheres were transported atop a tightly packed, flat bed in order to eliminate the role of bed protrusion and packing degree on the angle of repose of the mobile spheres (Papanicolaou et al., 2002). The flat packed bed was composed of two layers of spherical glass particles to allow flow development within the porous matrix (which can affect turbulent flow characteristics over the bed) and achievement of no-slip condition (Cooper et al., 2018; Papanicolaou & Kramer, 2005). The diameter of the spheres comprising the bed is denoted as $d_{bed} = d_{50} = 19.1 \text{ mm}$. This equality ensured that particles mostly travel along a straight path in the longitudinal direction of the flume bed (Steidtmann, 1982). Rigid balls with $d_c = 55 \text{ mm}$ were fixed atop the bed in a staggered arrangement with spacing of $\lambda = 6d_c$, to mimic boulders under the isolated roughness regime (Morris, 1955). This packing arrangement yielded negligible wake interactions between neighboring boulders and removed the importance of boulder packing density on bedload movement and trapping, as the focus here was to isolate the controls of each boulder within the array on bedload (Bunte & Poesen, 1993; Canovaro et al., 2007; Yager et al., 2007). Rectilinear flow was provided at the flume entrance by a curved flume headbox, in addition to a honeycomb, and the flow rate was monitored using an electronic flowmeter. Flow uniformity was attained in the test section by placing rods transversely to the flow at the tailgate and adjusting their number and height above the flat packed bed surface for each flow condition. Flow depths were verified at 2.0 m intervals along the length of the flume using rulers placed on the plexiglass flume sidewalls. The boulder array test section was placed 10.9 m downstream of the honeycomb entrance, where the flow was fully developed (Tsakiris, Papanicolaou, Hajimirzaie et al., 2014). The array test section was composed of 19 boulder rows (48 total boulders) distributed over a length of 5.2 m. This length ensured that fully adjusted flow conditions developed within the boulder array, which were estimated to occur within the first half of the array length for all tested flow conditions (Belcher et al., 2003; Papanicolaou et al., 2011). The flow adjustment length estimates are provided in Appendix A. The extensive number of boulder rows also allowed unique plan and side view observations of the morphological changes developing along the length of the boulder array.

The definition of relative submergence, which has been coined in the literature for a standalone submerged obstacle (see earlier definition in section 1), is modified here, for using it within the boulder array, by introducing the term $\langle H \rangle$, which denotes the reach-averaged flow depth within the array test section. The experimental sets therefore representing the two bookend cases, HRS and LRS within the array, are defined as $\langle H \rangle/d_c = 3.5$ and $\langle H \rangle/d_c = 0.8$ conditions hereafter. For each experimental set, stress conditions were selected based on the ratio, $\langle \tau_{o,ap} \rangle^*/\tau_{cr}^*$, between the reach-averaged, dimensionless, bed shear stress of the approach flow, $\langle \tau_{o,ap} \rangle^*$, and the dimensionless critical shear stress for incipient motion of median size bedload particles, τ_{cr}^* . Angle brackets denote a reach-averaged quantity. $\langle \tau_{o,ap} \rangle^*$ and τ_{cr}^* are defined as

$$\langle \tau_{o,ap} \rangle^* = \frac{\langle \tau_{o,ap} \rangle}{(\rho_s - \rho)gd_{50}}, \quad (1)$$

$$\tau_{cr}^* = \frac{\tau_{cr}}{(\rho_s - \rho)gd_{50}}, \quad (2)$$

where $\langle \tau_{o,ap} \rangle = \rho g \langle H_{ap} \rangle S_0$, $\langle H_{ap} \rangle$ denotes the reach-averaged approach flow water depth to the boulder array section, S_0 denotes the flume bed slope, ρ_s denotes the sediment density, ρ denotes the fluid density, and g denotes the gravitational acceleration. The critical shear stress for incipient motion of the median bedload material size, τ_{cr} , was determined experimentally with a set of separate tests. The tests replicated approach flow conditions, that is, conditions found well upstream of the entrance to the boulder array, where the effects of the array were negligible, and corresponded to the location along the flume length where feeding of the particles occurred. The critical stress experiments were carried out at 1% bed slope, which is an intermediate slope to the values used for the HRS and LRS conditions (Table 1). The critical stress was then calculated based on the probability of entrainment concept that incorporates the role of near-bed turbulence (i.e., moments of instantaneous drag and lift forces) on the estimation of entrainment of particles

Table 1
Key Experimental Parameters

Experimental set	Test	Reach-averaged, dimensionless, normalized approach			Time-averaged bedload feeding rate			Reach-averaged, dimensionless, normalized array grain shear stress			Constant time-averaged exiting bedload rate		
		$\tau_{o,ap}^*/\tau_{cr}^*$	S_0	Boulder relative submergence $\langle H \rangle/d_c$	$\bar{q}_{s,in}$	$\langle \tau_{gr} \rangle/\tau_{cr}^*$	Q	U_{bulk}	Froude number Fr	Reynolds number $Re \times 10^4$	$\bar{q}_{s,e}$ (g/m/s)		
HRS	1a	1.84	0.0024	3.5	0.942	1.08	0.134	0.76	0.56	58.66	0.244		
	1b	2.30	0.0030	3.5	1.515	1.08	0.134	0.76	0.56	58.66	0.174		
	2a	2.76	0.0036	3.5	2.152	1.51	0.138	0.78	0.57	60.20	0.411		
	3a	3.22	0.0042	3.5	2.961	1.51	0.137	0.78	0.57	60.08	0.463		
	3b	1.84	0.0159	0.8	0.942	1.89	0.144	0.82	0.60	62.93	1.173		
	4a	2.30	0.0186	0.8	1.515	1.94	0.141	0.80	0.59	61.74	1.137		
	4b	2.76	0.0212	0.8	2.152	2.32	0.147	0.84	0.61	64.29	1.768		
	4b	3.22	0.0239	0.8	2.961	2.34	0.146	0.83	0.61	64.03	1.665		
LRS	1a	1.84	0.0159	0.8	0.942	0.99	0.020	0.49	0.75	8.67	0.010		
	1b	2.30	0.0186	0.8	1.515	0.99	0.020	0.49	0.75	8.67	0.015		
	2a	2.76	0.0212	0.8	2.152	1.08	0.022	0.54	0.82	9.41	0.279		
	3a	3.22	0.0239	0.8	2.961	1.16	0.021	0.53	0.81	9.29	0.227		
	3b	1.84	0.0306	0.8	2.152	NA ^a	NA ^a	NA ^a	NA ^a	NA ^a	NA ^a		
	4a	2.30	0.0306	0.8	2.961	1.91	0.029	0.71	1.09	12.51	0.912		
	4b	2.76	0.0306	0.8	2.961	2.17	0.030	0.75	1.14	13.13	1.980		
	4b	3.22	0.0306	0.8	2.961	2.23	0.030	0.74	1.13	13.01	2.064		

Note: $\tau_{cr}^* = 0.0085$ is the dimensionless shear stress for incipient motion of d_{50} size particles (19.1 mm); $\langle \tau_{o,ap} \rangle = \rho g \langle H_{ap} \rangle S_0$, where $\rho = 998 \text{ kg/m}^3$ is the water density (at temperature, $T = 20^\circ\text{C}$) and $\rho_s = 2.545 \text{ kg/m}^3$ is the bedload material sediment density; $U_{bulk} = Q / (\beta \langle H \rangle)^{0.5}$; $Fr = U_{bulk} / (g \langle H \rangle)^{0.5}$, $Re = 4 \langle H \rangle U_{bulk} / \nu$, where $\nu = 1.004 \times 10^{-6} \text{ m}^2/\text{s}$ is the kinematic viscosity of water.

^aThis test replicate excluded because of error in the experimental duration.

Table 2
Bedload Feeding Material Characteristics

Particle diameter, d (mm)	Particle color	Size fraction (–)
8.0	Light Green	0.003
15.9	Blue	0.062
19.1	Orange	0.204
22.2	Emerald	0.461
25.4	Amber	0.270

(Papanicolaou et al., 2002). The determined critical dimensionless shear stress was $\tau_{cr}^* = 0.0085$. This τ_{cr}^* value, although it is significantly lower than the majority of values reported for natural-worn sediments (Buffington & Montgomery, 1997), compares well with previously reported values in the literature for spherical particles placed atop a tightly packed bed of unisized spheres (Coleman, 1967; Fenton & Abbott, 1977; Strom et al., 2004). The lower τ_{cr}^* value has been therefore attributed to the idealistic bed geometry with the well packed, nonprotruding bed found in the present experiments, the spherical shape of entrainable particles (Shape Factor of 1), and incorporation of the fluctuating component of drag and lift in the analysis for estimating the onset of movement (Elhakeem et al., 2016; Papanicolaou et al., 2002).

Using the ratio $\langle\tau_{o,ap}\rangle^*/\tau_{cr}^*$ as the basis of comparing bedload transport between HRS and LRS conditions, four approach flow stress conditions with $\langle\tau_{o,ap}\rangle^*/\tau_{cr}^* = 1.8, 2.3, 2.8$, and 3.2 were selected. These ranges correspond to typical bankfull flow and general sediment movement conditions (Pitlick et al., 2008). To attain the same $\langle\tau_{o,ap}\rangle^*/\tau_{cr}^*$ values for the HRS and LRS test sets, the flume slope and flow rate were adjusted accordingly (Table 1). In each experimental set, two identical tests were conducted at every flow condition to ensure repeatability (with an exception at the LRS-3 condition due to an error in the experimental duration of one replicate). The key experimental parameters for all tests are summarized in Table 1.

Bedload material was fed to the flume approach section, during each test, at a location that was 4 m upstream of the boulder array entrance. A sediment diffuser was utilized to ensure uniform feeding of particles across the flume width (Papanicolaou et al., 2011). The feed material was composed of five size fractions of spherical glass beads in the bedload distribution outlined in Table 2, where each size class had a distinct color to aid visual assessment of bedload transport and deposition per size fraction. The proportions in this distribution were selected to mimic the transported bedload material of Oak Creek, Oregon, which followed a negatively skewed log-normal distribution (Diplas, 1987). The supplied material had a geometric standard deviation of 1.26. Because the bed was tightly packed and the mobile material was too large to infiltrate the bed, exchanges between the bed and the mobile sediment were absent. In addition, mobile material was only able to deposit in a single layer atop the immobile bed. Thus, the effects of vertical sorting as well as consecutive armor layer formation and destruction, which were present in the Ghilardi et al. (2014a, 2014b) study, were eliminated.

For each stress condition, the bedload feeding rate was estimated according to the formula $\overline{q}_{s,in}^* = C(\tau^*)^2$, where $\overline{q}_{s,in}$ denotes the time-averaged incoming bedload rate per unit width in cubic meter per meter per second, $\overline{q}_{s,in}^*$ denotes the dimensionless version of $\overline{q}_{s,in}$ (i.e., $\overline{q}_{s,in}^* = \overline{q}_{s,in}/[g(\rho_s/\rho - 1)d_{50}^3]^{0.5}$), τ^* denotes the dimensionless shear stress available for mobilizing sediment, and C is an empirical constant that is equal to 0.15. This bedload relation was chosen to be similar to the one developed by Strom et al. (2004), who employed an experimental bed geometry and flow conditions similar to the present study. This choice was based on the presumption that the effects of stable clusters (i.e., patches of grouped particles) on incoming bedload in the Strom et al. (2004) experiments would be similar to the effects of boulders in the present experiments. The bedload feeding rates, $\overline{q}_{s,in}$, were found using $\langle\tau_{o,ap}\rangle^*$ in the above equation and are reported in Table 1.

To ensure a consistent size distribution of incoming material throughout the duration of a run, bedload was fed in premade batches of mixed size fractions specified in Table 2. The feeding intervals of 5, 5, 2.5, and 2 min were used for the stress conditions $\langle\tau_{o,ap}\rangle^*/\tau_{cr}^* = 1.8, 2.3, 2.8$, and 3.2, respectively. These timing intervals were experimentally determined based on estimates of travel times through the array (accounting for both movement and resting). The potential role of bedload feeding intervals on bedload fluctuations for the $\langle H \rangle/d_c = 3.5$ and $\langle H \rangle/d_c = 0.8$ is discussed in section 3.

Observational data of bedload transport and deposition were made in the forms of (1) video camera observation at the downstream exit of the boulder array throughout each test; (2) plan view photos taken of the entire array at the conclusion of each test; and (3) close-up, side-view photos and short-clip video taken semi-regularly at representative locations along the boulder array. The time series of instantaneous exiting bedload rates, $q_{s,e}$, from the array were determined from analyzing videos by recording the time of exit for

different size particles, which were differentiated according to color. Particle exit times were estimated via video every second through differences of consecutive images (30 images per second), but were subsequently binned to 10-s sampling to reduce particle counting errors. For instance, this 10-s sampling represents a multiple of the average travel time required for a particle to travel downstream at a distance equal to the streamwise spacing between boulders (Julien & Bounvilay, 2012; Knapp, 2002; Papanicolaou et al., 2009). From this record of exiting particles, the exiting size fraction distributions were also constructed in order to compare with the distributions of the feeding material (i.e., Table 2). The incoming and exiting distributions were similar for the HRS tests, but the exiting bedload was slightly coarser than the incoming bedload for the LRS test set (see Figure S1 for distribution plots). For all LRS tests, however, the exiting d_{50} was less than 7% greater than the incoming d_{50} .

The tests had a 95-min total duration except the LRS-4 tests, which were of 60-min duration. The duration for all tests was deemed sufficient for recording both short and large bedload fluctuation timescales (Papanicolaou et al., 2011). This duration was also sufficient to reach a constant time-averaged, or mean, value of $q_{s,e}$ in each test, which is denoted as $\bar{q}_{s,e}$. To determine $\bar{q}_{s,e}$, the $q_{s,e}$ time series were first rebinned at 5-min sampling intervals (equal to the largest feeding period interval). In these time series, $q_{s,e}$ was typically very low near test commencement (due to initially high rates of bedload entrapment by the array), then increased over the first 15–30 min of the test, and finally leveled to fluctuate around a relatively constant $\bar{q}_{s,e}$ for the remainder of the test (Supporting Information Figure S2). Thus, $\bar{q}_{s,e}$ was calculated for each test by taking the time average of $q_{s,e}$ between the time of the first $q_{s,e}$ peak after the initial increase and the end of the test. The constant $\bar{q}_{s,e}$ magnitudes are given in Table 1. In terms of test repeatability, the values of $\bar{q}_{s,e}$ for two identical tests varied from about $\pm 18\%$ of the average at the lowest stresses to about $\pm 3\%$ at the highest stresses for both the HRS and LRS sets. The higher variability during the lowest stresses was attributed to near-bed turbulent fluctuations (Papanicolaou et al., 2002). At the highest stresses the contributions of turbulent fluctuations were comparable in magnitude to the average bed shear stress.

To estimate the reach-averaged shear stress portion available to mobilize bedload particles (or grains) within the array, $\langle \tau_{gr} \rangle$, a similar approach to Yager et al. (2007) was considered. The stress exerted on bedload grains is expressed as

$$\langle \tau_{gr} \rangle = \frac{\langle \tau_t \rangle A_t - \langle \tau_l \rangle A_{lp}}{A_m}, \quad (3)$$

where A_t denotes the total bed area, A_{lp} denotes the bed-parallel area occupied by immobile boulders, A_m denotes the bed area available to transport mobile sediment ($=A_t - A_{lp}$), $\langle \tau_t \rangle = \rho g \langle H \rangle S_0$ is the reach-averaged total shear stress within the array, and $\langle \tau_l \rangle = \rho A_{lp} C_d U_{d_c}^2 / (2A_{lp})$ is the reach-averaged stress borne by immobile boulders in the array. A_{lp} denotes the bed-perpendicular area of immobile boulders, U_{d_c} denotes the boulder approach velocity averaged over the boulder height (see Appendix B), and C_d denotes the drag coefficient of the boulders.

Determination of C_d was performed for three representative groups of experimental flow conditions: (1) HRS, (2) LRS with Froude number, $Fr < 1$, and (3) LRS with $Fr > 1$ (see section 3.1 for more details). These three conditions were identified based on the recognition that for LRS with $Fr < 1$, C_d is highly dependent on Fr (e.g., see Figure 2 in Flammer et al., 1970). C_d values were then estimated for each group by minimizing the root-mean-square error of unit flow discharge, q , predictions from methods similar to Yager et al. (2007; for further details, see Appendix C). The corresponding C_d values for these groups are equal to 0.70, 1.73, and 0.84, respectively, and provided q prediction errors less than 11% for all experiments. The C_d of 0.70 for the HRS set corresponds closely with the value of 0.73 reported by Schmeeckle et al. (2007) for a sphere at HRS conditions. For the LRS set, however, $C_d = 1.73$ was determined when $Fr \approx 0.8$ and $C_d = 0.84$ was determined when $Fr \approx 1.1$ (Table 1). These C_d magnitudes and dependence on Fr in the present LRS set are in good agreement with the findings of Flammer et al. (1970). Their study, conducted for a hemisphere with diameter $d_c = 6.4$ cm showed that C_d was about 2.4 at $Fr = 0.8$ when the relative submergence of the hemisphere, defined therein as $\langle H_{ap} \rangle / (1/2 d_c)$, was equal to 0.8. At this submergence, the C_d proceeded to drop rapidly with increasing Fr , achieving a value of 1.0 at about $Fr = 1.2$, and then started approaching a minimum near 0.35 by about $Fr = 2.0$. The fitted C_d magnitudes were considered in the calculations of $\langle \tau_{gr} \rangle$ via equation (3). The $\langle \tau_{gr} \rangle$ values determined for each test are reported in Table 1.

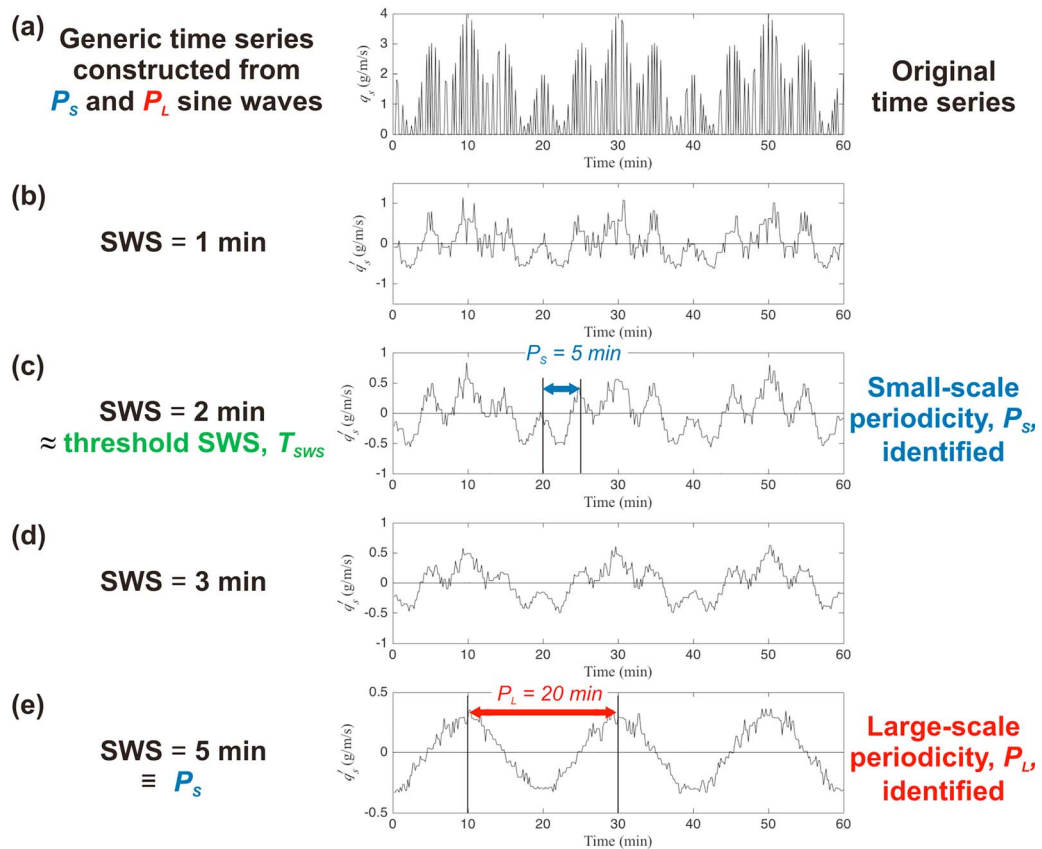


Figure 1. Illustration showing the identification of bedload fluctuation timescales in a generic time series using moving average filters with different SWS. (a) The original time series of exiting bedload transport, $q_{s,e}$, generated from sine waves with P_S of 5 min and P_L of 20 min; and (b)–(e) smoothed fluctuations about the time average, $q_{s,e}'$. SWS = smoothing window size; P_S = small-scale periodicity; P_L = large-scale periodicity.

2.2. Bedload Timescale Analyses

The methodological steps followed for the timescale analyses are illustrated in Figure 1 for a generic time series of the instantaneous $q_{s,e}$. The generic time series of the raw bedload data, shown in Figure 1a, are constructed from two superimposed sine waves, the timescales of which are termed herein as the small-scale periodicity, P_S , and the large-scale periodicity, P_L . Note that in the generic time series of Figure 1a, P_S and P_L are camouflaged by sparse sampling that had many intermediate values equal to zero due to the discrete exiting bedload. Therefore, steps to discern P_S and P_L from the raw data are described below. Figures 1b–1e depict how moving average filters with increasing smoothing window sizes (SWS) can be used to identify both P_S and P_L in the generic time series. Smoothing with a moving average is performed by replacing a data point with the average of its neighboring data points, within a given SWS, and then applying this windowed averaging to all sequential segments of the original time series. Figure 1b for example shows that when SWS is equal to 1 min, undulations likely associated with sparse sampling effects remain and not all of the P_S peaks are easily discerned. However, when SWS becomes equal to 2 min (Figure 1c), the sparse sampling effects are removed and all P_S peaks are clearly identified. This specific SWS is denoted herein as the threshold window size, T_{SWS} , which is employed to identify P_S . As the SWS is subsequently increased above the threshold value, T_{SWS} , (see Figures 1d–1e) the P_S pulsations become progressively smoothed and the large-scale periodicity, P_L , pulsations are seen more clearly. Figure 1e shows how smoothing with SWS that equates to P_S can be used to identify fluctuations at the larger superimposed timescale, P_L .

While commonly used to smooth fast fluctuations in a time series, the moving average method is generally recognized to be a qualitative method as subjectivity exists in the selection of an appropriate SWS (e.g., Cryer & Chan, 2008; Cudden & Hoey, 2003; Fox et al., 2005). To remove some of the subjectivity in estimating P_S and

P_L from the moving average analysis, our analysis was complemented with a more quantitative approach. This approach involved two methodological steps to discern both timescales: (1) determination of the small-scale periodicity, P_S , using the pulse period (PP) method of Cudden and Hoey (2003); and (2) determination of the large-scale periodicity, P_L , using the normalized autocorrelation function of the smoothed fluctuating bedload time series (Ghilardi et al., 2014b). These methodological steps are presented in subsections 2.2.2 and 2.2.3, respectively, after discussing the prerequisite step of detrending the nonstationary mean bedload rate from the bedload time series in subsection 2.2.1.

2.2.1. Detrending Nonstationary Mean Bedload Rate Prior to P_S and P_L Estimation

A necessary step, prior to isolating the P_S and P_L fluctuations in $q_{s,e}$ with the predetermined two methodological steps, was to remove the nonstationary increase in the mean exiting bedload rate. To evaluate the nonstationary mean, a sampling period that is equal or greater than the T_{SWS} (i.e., see section 2.2.2 for details) was selected to ensure the effects of sparse sampling were minimal. In this study, this sampling period was arbitrarily selected to be equal to 3 min. The nonstationary mean was evaluated using linear regression, and statistical significance of the fitted slope was subsequently tested by the p value. If the regression was found to be significant (95% confidence), the fitted equation for the 3-min time series was considered to be suited for describing the nonstationary in the observed 10-s time series. Thus, the original 10-s bedload time series, $q_{s,e}(t)$, was decomposed by $q_{s,e}(t) = \bar{q}_{s,e}^{ns}(t) + q_{s,e}'(t)$, where $\bar{q}_{s,e}^{ns}(t)$ is the nonstationary mean bedload rate calculated from the regression equation at time t and $q_{s,e}'(t)$ is the fluctuating component of the bedload time series (e.g., Strom et al., 2004). If the linear regression was found to be insignificant, $\bar{q}_{s,e}^{ns}(t)$ was considered to be the time-averaged bedload rate throughout the entire test duration. The fluctuating component of the bedload time series, hereafter denoted as $q_{s,e}'$, was used in subsequent timescale analyses. In general, $q_{s,e}'$ is useful for highlighting time periods when bedload rates are greater than (positive $q_{s,e}'$) or less than (negative $q_{s,e}'$) the mean.

2.2.2. Determination of the Small-Scale Periodicity, P_S

To objectively select an appropriate SWS, the PP method of Cudden and Hoey (2003) was implemented. The PP method allows (1) selection of the threshold value, T_{SWS} , which identifies the small-scale pulsating structure of the time series and (2) determination of the P_S timescale magnitude that characterizes these bedload rate pulsations. P_S is equivalent to the dominant period timescale in the original method of Cudden and Hoey (2003).

The PP method was employed herein to investigate the characteristic changes in the average timescale of $q_{s,e}'$ fluctuations as a function of changing SWS. The timescale of fluctuations was quantitatively estimated for a given SWS by the PP value, which was defined as the average time period between successive peaks in the time series. PP was thus calculated as the total time series duration divided by the number of time series peaks, or local maxima (e.g., Hoey, 1992). In order to account for signal noise when detecting the time series peaks, an algorithm using the first-derivative crossing method was used (e.g., O'Haver, 1991). As an outcome from these steps, plots of PP versus SWS were generated and used in subsequent analysis. Considering PP as a function of SWS, PP was generally expected to increase initially with increasing SWS when the fast fluctuations in the time series were progressively removed. However, above T_{SWS} the fast fluctuations in the time series were expected to be fully removed, causing PP to stabilize around a constant value (Cudden & Hoey, 2003; Hoey, 1992). The SWS where the PP initially stabilized was interpreted of T_{SWS} from this method, which is denoted as $T_{SWS,PP}$. Finally, the stable PP value was taken as the P_S magnitude.

To validate the value of T_{SWS} determined with the PP method, a second independent method based the skewness (Sk), that is, the third statistical moment, of the time series was employed. Past research on turbulent velocity time series has outlined this method and shown that Sk versus SWS exhibited significant changes (e.g., significant slope changes, zero crossings) at T_{SWS} (Fox et al., 2005; Tamburino & Gulliver, 1999). The T_{SWS} values determined with this method were denoted as $T_{SWS,Sk}$ and were compared with $T_{SWS,PP}$ for validation.

2.2.3. Determination of the Large-Scale Periodicity, P_L

To isolate the larger timescale of $q_{s,e}'$ when multiple timescales are present, it is shown that the chosen SWS value is optimal when it becomes equal to the smaller fluctuation timescale (e.g., Figure 1e). Therefore, each $q_{s,e}'$ was filtered using SWS equal to the previously determined P_S timescale in order to reveal the larger

timescale of fluctuations, P_L . Using similar methods to Ghilardi et al. (2014b) for quantitative estimation of P_L , the normalized autocorrelation function of $q_{s,e}'$, $A_{qs}(\delta)$, was employed. $A_{qs}(\delta)$ is calculated as

$$A_{qs}(\delta) = \int_0^{T-\delta} \frac{q_{s,e}'(t)q_{s,e}'(t+\delta)}{\sigma_{q_{s,e}}^2} dt, \quad (4)$$

where δ is the lag time, T is the total test duration, and $\sigma_{q_{s,e}}^2$ is the time series variance. When considering time series smoothed with P_S , $A_{qs}(\delta)$ was expected to exhibit a peak at the δ corresponding to the P_L timescale magnitude (Ghilardi et al., 2014b). To ensure that smaller peaks were not erroneously selected, the first statistically significant peak (using 95% confidence limits) in the $A_{qs}(\delta)$ plot was interpreted as the timescale estimate for P_L . Additional peaks occurring repetitively at or near multiples of P_L were also used to confirm the selected timescale.

3. Results

This section presents the experimental results detailing the effects that the boulder array has on incoming bedload from three different, yet complementary, perspectives examined in the following subsections. Subsection 3.1 offers a qualitative assessment of the role of boulder submergence and Froude number on the bed morphological characteristics around them, including the location and size of the formed depositional patches (specific objective 1, see section 1). Subsection 3.2 documents the effects of the boulder array on mean bedload rates $\bar{q}_{s,e}$ (specific objective 2). Such analysis allows comparison of the $\bar{q}_{s,e}$ values obtained in each test with literature findings and assessment of the mean bedload trapping rates, $\bar{q}_{s,trap}$, to aid isolation of the role of the array on mean bedload. Subsection 3.3 complements this analysis and examines the effects that the boulder array has on fluctuation timescales in the exiting bedload transport rate (specific objective 3). Due to space considerations, selected results from one test at each flow condition are presented. For HRS these are tests 1a, 2a, 3a, and 4b and for LRS these are tests 1b, 2b, 3b, and 4b.

3.1. Bed Morphological Characteristics

The bed morphological characteristics that developed by bedload deposition within the boulder array were assessed from plan view images taken at the conclusion of selected experimental tests from each flow condition. These images are presented for all flow conditions in the HRS set in Figure 2 and for the LRS set in Figure 3 (as well as available images of test replicates are provided in Figures S3 and S4 for the HRS and LRS sets, respectively). In the following, the systematic patterns of bed morphology are analyzed first with reference to the location around individual boulders and second with reference to the location in the boulder array.

For all HRS tests, the deposition of incoming bedload occurred primarily in individual boulder wake regions and to a lesser extent in the areas in-between neighboring boulders. Some deposition also occurred in the low-shear region along the flume sidewalls and was attributed to Prandtl's second kind of secondary currents. These secondary currents, generated from the boulders presence, entrained particles laterally and toward the flume wall (Papanicolaou, 2012). The observed bed morphology, characterized primarily by deposition of mobile material in the wake of other stationary particles, is consistent with observations from both field and laboratory studies at HRS conditions (Brayshaw, 1984; Bunte & Poesen, 1993; Strom et al., 2004). By examining local hydrodynamics, bedload deposition in this region has been attributed to the near-wake recirculation of the mean flow and the drastic reduction in local bed shear stress available to mobilize sediment (Dey et al., 2011; Papanicolaou et al., 2012; Shamloo et al., 2001).

The local bed morphology developed in the LRS tests (Figure 3) was instead marked by bedload deposition predominantly upstream of individual boulders, which presents a direct contrast with the HRS tests. This type of upstream depositional morphology is not well documented in literature, and to the authors' knowledge very few researchers (e.g., Monsalve & Yager, 2017; Papanicolaou et al., 2011; Papanicolaou & Kramer, 2005) have connected deposition upstream of boulders with partial submergence flow conditions, whereas other studies have typically connected this behavior with imbrication (e.g., Brayshaw, 1984; Laronne & Carson, 1976). We attribute the deposition of the material upstream of the boulders to the necklace structure

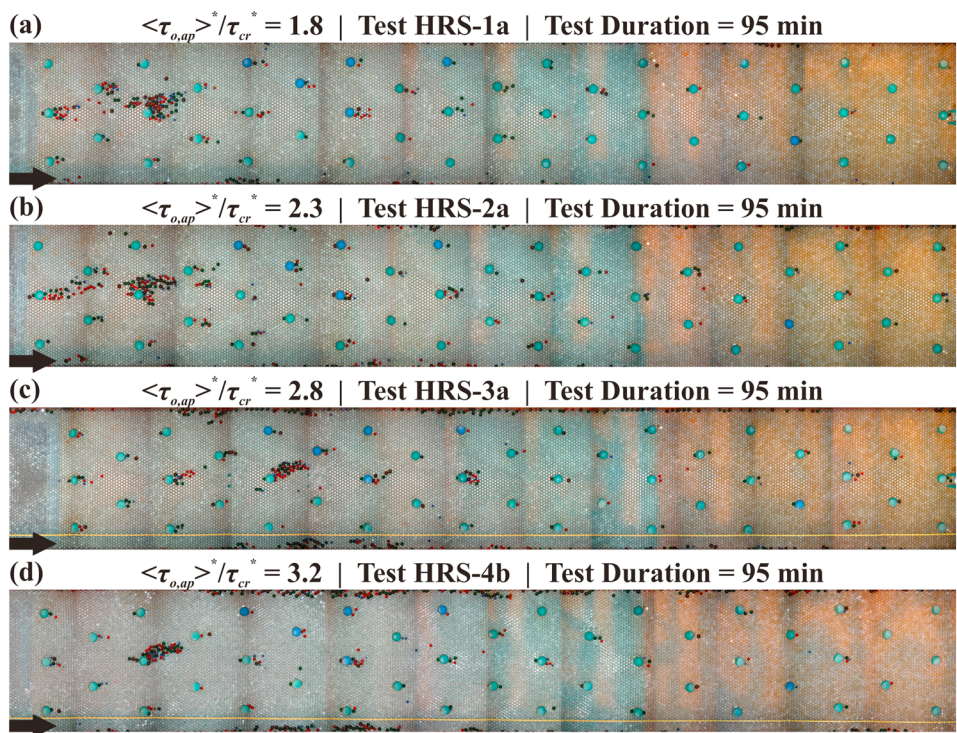


Figure 2. Plan view images of the boulder array and deposited material at the conclusion of HRS tests selected from each tested flow condition. (a) Test HRS-1a; (b) test HRS-2a; (c) test HRS-3a; and (d) test HRS-4b. The boulders found at the array entrance are shown at the far left hand side of the images; black arrows indicate flow direction. HRS = High Relative Submergence.

of the horseshoe vortex (HSV) that develops at the leading edge of the boulders, where the flow usually oscillates between the zero velocity and backflow mode (Paik et al., 2007).

A more thorough examination of Figure 3 further highlights an apparent location change in the local depositional morphology within the LRS test set, which occurred between the second and third stress conditions. Indeed, at the lower two stresses, $\langle \tau_{o,ap} \rangle^*/\tau_{cr}^* = 1.8$ and 2.3, bedload mainly deposited in the stoss region of boulders (Figures 3a–3b). On the contrary, at the higher two stresses, $\langle \tau_{o,ap} \rangle^*/\tau_{cr}^* = 2.8$ and 3.2, bedload primarily deposited in patches located at the upstream flanks of boulders (Figures 3c–3d). Investigating the cause of this behavior within the LRS test set, a direct correspondence between this morphological change and a hydraulic regime change from subcritical ($Fr < 1$) to supercritical ($Fr > 1$) flow is observed (Table 1). Furthermore, the linkage between this flow regime change and the bed morphological changes is elucidated by qualitatively examining the different types of surface wave features that occurred around boulders at LRS for both $Fr < 1$ and $Fr > 1$. Figure 4 first illustrates the two types of wave characteristics that were common at LRS for both Fr regimes: (1) standing waves with a wavelength corresponding with the boulder down-stream spacing and (2) local depressions occurring just downstream of individual boulders. Second, Figure 4 highlights the key difference in wave features between these regimes, which is the presence of local wave crests (LWCs) at the upstream flanks of individual boulders occurring uniquely in the $Fr > 1$ regime. The locations of these LWCs at $Fr > 1$ corresponded with the patch locations of deposited bedload (Figure 4). These findings are similar to the study of Boyer and Roy (1991), who observed distinct sand bed scour geometries around a hemisphere for subcritical and supercritical flows. At supercritical flow, their study highlighted sediment deposition along the flanks of the obstacle, which resemble the patterns exhibited herein at similar conditions (i.e., Figures 3c–3d).

Based on the preceding analysis, the present experiments overall suggest that local bed morphological characteristics around boulders are controlled by two parameters indicative of the flow hydraulics, namely, the boulder relative submergence and the Froude number. Some of the effects that these parameters have on obstacle controls to flow and sediment have been reported in previous studies (Boyer & Roy, 1991;

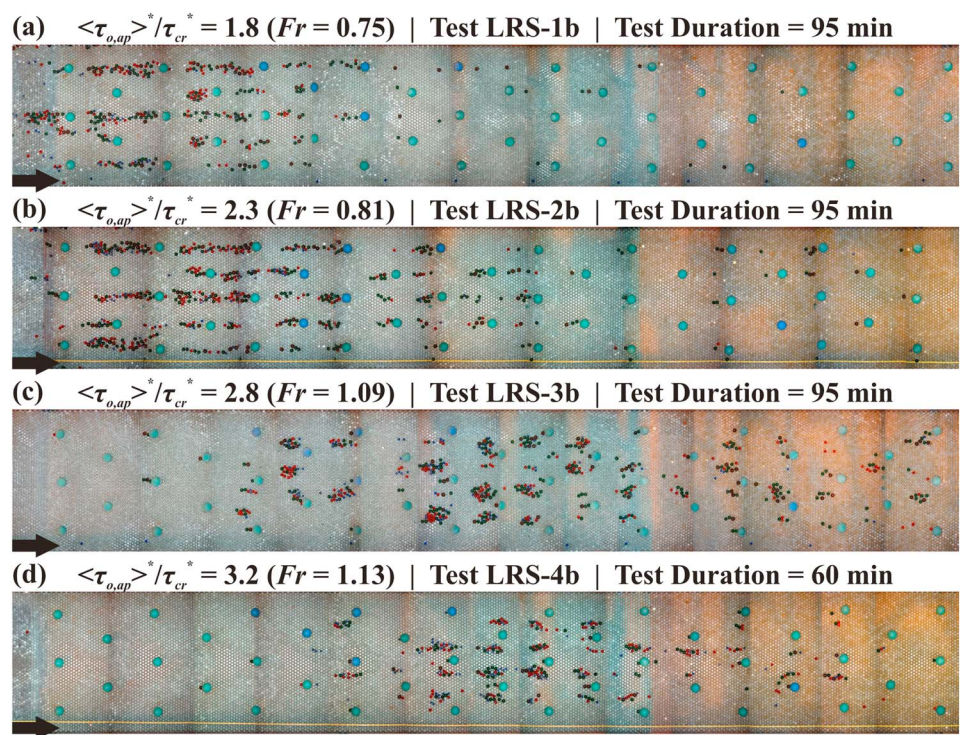


Figure 3. Plan view images of the boulder array and deposited material at the conclusion of LRS tests selected from each tested flow condition. (a) Test LRS-1b; (b) test LRS-2b; (c) test LRS-3b; and (d) test LRS-4b. The boulders found at the array entrance are shown at the far left hand side of the images; black arrows indicate flow direction. LRS = Low Relative Submergence.

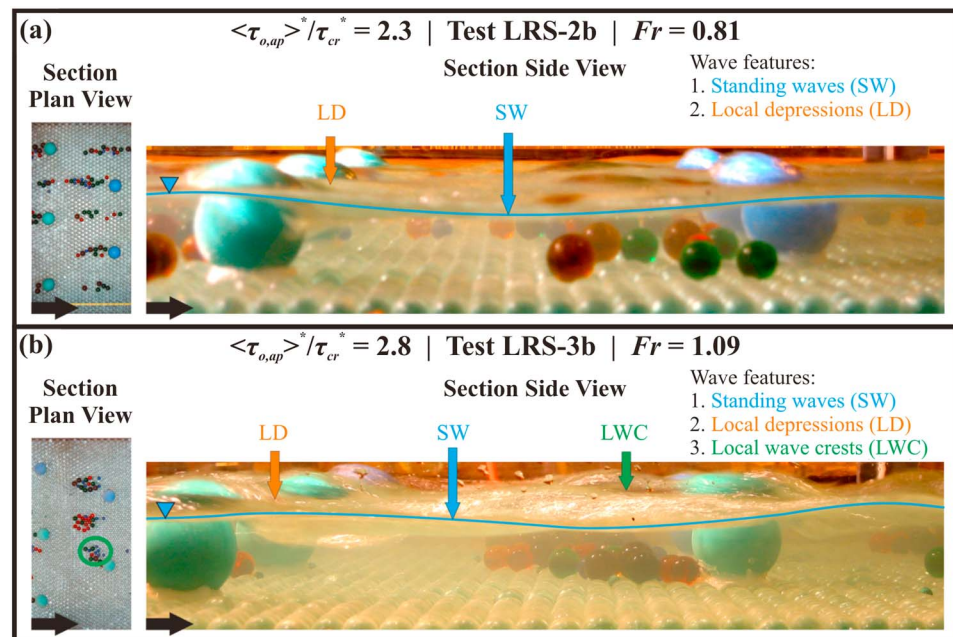


Figure 4. Wave features for LRS shown in connection with plan view images of deposition. (a) Test LRS-2b with $Fr < 1$; and (b) test LRS-3b with $Fr > 1$. Examples of SW and LD are indicated in both (a) and (b); a LWC and the corresponding depositional patch are indicated in the side and plan view images, respectively, in (b); black arrows indicate flow direction. LRS = Low Relative Submergence; SW = standing waves; LD = local depressions; LWC = local wave crests; Fr = Froude number.

Papanicolaou & Tsakiris, 2017; Riviere et al., 2017). From the directly comparable tests herein, however, three distinct cases of local depositional morphology around boulders are uniquely discerned and linked to $\langle H \rangle / d_c$ and Fr :

Case 1: Material deposits in the wake (downstream) region of a boulder controlled by the near-wake recirculation and reduction in local bed shear stress

$$\begin{aligned}\langle H \rangle / d_c &= 3.5 \text{ (HRS)} \\ Fr &< 1.\end{aligned}$$

Case 2: Material deposits in the stoss (upstream) region of a boulder controlled by the HSV and in the decelerated flow zone developed immediately downstream of the local depression

$$\begin{aligned}\langle H \rangle / d_c &= 0.8 \text{ (LRS)} \\ Fr &< 1.\end{aligned}$$

Case 3: Material deposits at the upstream flanks of boulders mostly controlled by the location of the LWCs in the boulder vicinity

$$\begin{aligned}\langle H \rangle / d_c &= 0.8 \text{ (LRS)} \\ Fr &> 1.\end{aligned}$$

Building from the above descriptions of local bed morphology around individual boulders, the locations of bedload deposition within the boulder array reach are also investigated. For the Case 1 morphology (HRS), the majority of deposition accumulated roughly within the first five boulder rows in the array (Figures 2a–2d). These accumulations primarily occurred in large wake region patches along the flume centerline and along the flume sidewalls. For the Case 2 morphology (LRS with $Fr < 1$), incoming sediment also deposited in the entrance of the boulder array, albeit throughout a longer length compared to Case 1 (Figures 3a–3b). A similar finding to these characteristics of Cases 1 and 2 was reported by Bacchi et al. (2014), who noted that the majority of bedload deposition occurred near the flume entrance for experiments conducted with subcritical flow at an intermediate relative submergence for coarse gravel (i.e., $\langle H \rangle / d_{84} = 1.2$ and 1.9). It is possible that deposition at the array entrance for these two conditions is attributed to the transitioning flow characteristics within this region (e.g., Belcher et al., 2003). In contrast, bedload deposition within the boulder array in the Case 3 morphology (LRS with $Fr > 1$) presents a different behavior than the prior two cases. Nearly no bedload deposited within the first 4–6 rows of boulders in the array and the depositional patches began developing only after this length (Figures 3c–3d). In fact, the majority of deposition occurred in the midsection of the boulder array reach for Case 3. Considering more closely this behavior for the Case 3 morphology, observations reveal a qualitative connection between bedload deposition and LWCs that is similar to the local scale observations (i.e., Figure 4). In particular, Figure 5 shows that local flow features such as LWCs were not present in the first few boulder rows in the array and that there was no deposition of particles within this section of the array reach. Furthermore, Figure 5 shows that the location where these LWCs were developed closely matched the length within the array at which bedload deposition was first observed.

3.2. Mean Bedload Transport and Trapping Rates

The effects of the boulder array on mean bedload transport rates was first assessed by comparing the mean incoming and exiting bedload rates, $\bar{q}_{s,in}$ and $\bar{q}_{s,e}$, respectively (Table 1). This comparison revealed that the boulder array generally acted as a bedload sink, in the present experiments, by trapping incoming particles and reducing the mean bedload rate conveyed downstream by nearly 30–99%. Similar findings have been reported by previous researchers, who have attributed decreased bedload rates within a boulder array to the reduction of available grain shear stress because of boulder form drag (Ghilardi et al., 2014a; Papanicolaou et al., 2011; Yager et al., 2007).

To illustrate the role of boulders on conveyance and mean bedload rates, Figure 6a is populated with the current experimental data (filled, colored symbols) and literature data sets with nearly identical setups using

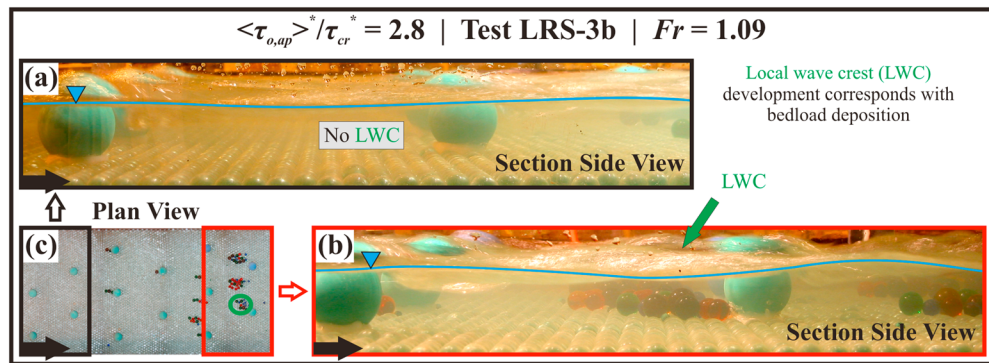


Figure 5. (a) Side view of wave features at the array entrance; (b) side view of wave features at the fifth–sixth boulder row; and (c) plan view of depositional locations within the first six rows of boulders in the array. A LWC and the corresponding depositional patch are indicated in (b) and (c), respectively; black arrows indicate flow direction. LRS = Low Relative Submergence; LWC = local wave crests; Fr = Froude number.

spheres atop a well-packed bed. In Figure 6a, $\overline{q_{s,e}}$ is normalized as $\overline{q_{s,e}^*} = \overline{q_{s,e}} / [g(\rho_s/\rho - 1)d_{50}^3]^{0.5}$ and is plotted as function of the reach-averaged excess dimensionless grain shear stress, $\langle\tau_{gr}\rangle^* - \tau_{cr}^*$ (where $\langle\tau_{gr}\rangle^* = \langle\tau_r\rangle^*$ was used for literature data in the absence of boulders). Overall, two groups of data are plotted in Figure 6a. The first group of data is comprised from published experiments with glass spheres atop a well packed bed without boulders (Papanicolaou & Knapp, 2010; Tsakiris, Papanicolaou, & Lauth, 2014). The second group is composed with data points from the present boulder experiments. Also, in this group the Strom et al. (2004) data were employed, which correspond to similar ranges of flow conditions with the current experiments. It is assumed that the *stable particle clusters* formed in the Strom et al. (2004) experiments play a similar role on bedload conveyance as boulders do. Henceforth, we consider that the role of the formed stable clusters in bearing stress is comparable to boulders, that is, the integrated drag over a stable cluster is of comparable magnitude to drag exerted by a boulder (Papanicolaou & Schuyler, 2003). The collapse shown in the reported boulder data with the Strom et al. (2004) results supports the above consideration. Overall, Figure 6a shows that the mean bedload in the presence of boulders (or of the equivalent boulders) is less in magnitude than in the absence of bed patchiness.

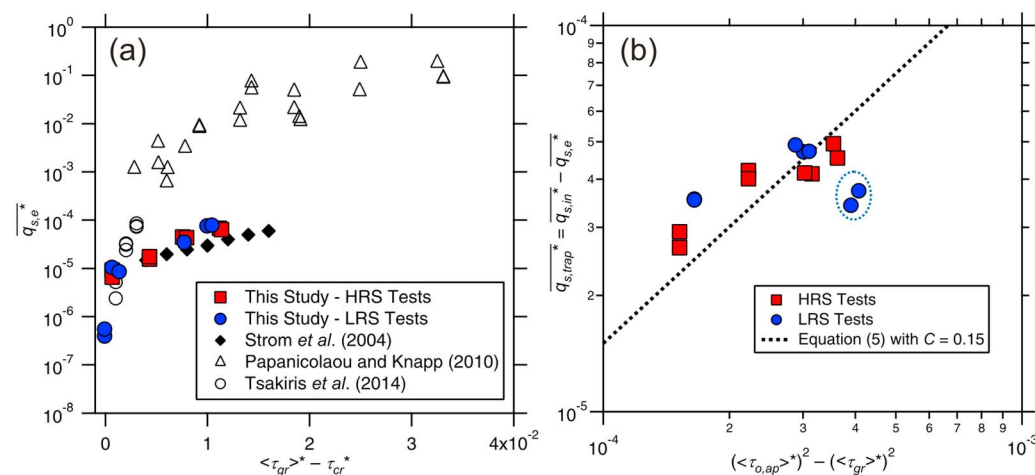


Figure 6. (a) Comparison of the dimensionless mean exiting bedload transport rates, $\overline{q_{s,e}}$, with literature using the reach-averaged, excess dimensionless grain shear stress, $\langle\tau_{gr}\rangle^* - \tau_{cr}^*$; and (b) the dimensionless mean bedload trapping rates, $\overline{q_{s,trap}^*}$, by the boulder array presented as a function of the difference between the reach-averaged, dimensionless approach flow shear stress, $\langle\tau_{o,ap}\rangle^*$, and the reach-averaged, dimensionless grain shear stress, $\langle\tau_{gr}\rangle^*$, both squared; circled points are from the LRS tests at $\langle\tau_{o,ap}\rangle^*/\tau_{cr}^* = 3.2$ (see discussion in section 3.2 for further detail). HRS = High Relative Submergence; LRS = Low Relative Submergence.

In order to quantify the role of the boulder array as a sink to incoming bedload, the dimensionless rate of bedload trapping, $\overline{q}_{s,trap}^*$, was also investigated using the current experimental tests (Figure 6b). By virtue of sediment continuity, $\overline{q}_{s,trap}^*$ is defined as the difference between $\overline{q}_{s,in}^*$ and $\overline{q}_{s,e}^*$. In order to predict the magnitudes of $\overline{q}_{s,trap}^*$, it is first recalled that $\overline{q}_{s,in}^*$ was calculated according to the equation $\overline{q}_{s,in}^* = C(\langle \tau_{o,ap} \rangle^*)^2$, with C equal to 0.15 (see section 2.1). Moreover, the experimental $\overline{q}_{s,e}^*$ values presented in Figure 6a closely follow the equation $\overline{q}_{s,e}^* = C(\langle \tau_{gr} \rangle^*)^2$, with C also equal to 0.15 ($R^2 = 0.839$). Therefore, $\overline{q}_{s,trap}^*$ may be estimated as

$$\overline{q}_{s,trap}^* = \overline{q}_{s,in}^* - \overline{q}_{s,e}^* = C[(\langle \tau_{o,ap} \rangle^*)^2 - (\langle \tau_{gr} \rangle^*)^2]. \quad (5)$$

Figure 6b incorporates the measurement-derived $\overline{q}_{s,trap}^*$ data and the corresponding estimates deduced via equation (5) when $C = 0.15$. Excluding the low $\overline{q}_{s,trap}^*$ values for the LRS tests at $\langle \tau_{o,ap} \rangle^*/\tau_{cr}^* = 3.2$ (points circled in blue in Figure 6b), the data points collapse onto a single line. The lower $\overline{q}_{s,trap}^*$ values at LRS with $\langle \tau_{o,ap} \rangle^*/\tau_{cr}^* = 3.2$ are attributed to the limited storage space available within the array to entrap bedload for this test (i.e., Figure 3d), which was dictated by the area occupied by the LWCs (i.e., Figure 4b).

3.3. Bedload Characteristic Timescales

3.3.1. The Role of Bedload Feeding Period on Bedload Pulsation

Before performing time series analyses to discern P_S and P_L , the potential effects of the experimental bedload feeding period on the exiting bedload time series must be assessed. To do so, the temporal autocorrelation function of equation (4) is applied to the original bedload time series (Figure 7). A 30-s sampling instead of the usual 10-s sampling is used because it aggregates particles exiting the array in close groups and aids assessing the direct connection of feeding and exiting pulse timing. For the HRS tests, Figure 7 shows that only a few $A_{qs}(\delta)$ values are statistically significant (95% confidence). These $A_{qs}(\delta)$ values do not coincide with the bedload feeding period and show no discernible trends with the stress condition in either lag location or correlation magnitude. Considering the LRS tests in Figure 7, however, statistically significant peaks of $A_{qs}(\delta)$ are identified at the bedload feeding period for each test. This coincidence is evidence of the influence that the bedload feed period has on exiting bedload. Furthermore, peak $A_{qs}(\delta)$ values of similar magnitude occur at all multiples of the feeding period, which shows the persistent influence of feeding pulses on exiting bedload throughout the duration of LRS tests. In a nutshell, the trends in Figure 7 suggest that the bedload feeding period is reflected in the temporal structure of exiting bedload time series at LRS conditions but not at HRS conditions.

3.3.2. Small-Scale Periodicity, P_S

In order to identify the presence of bedload rate fluctuations at the P_S timescale, PP is presented as a function of SWS in Figures 8 and 9 for selected tests at each flow condition from the HRS and LRS sets, respectively.

For all HRS tests (Figure 8), the PP plots followed the expected behavior, which had also been observed by Cudden and Hoey (2003). Namely, PP initially grew in magnitude with increasing SWS and then stabilized to a more constant value when the fast fluctuations in $q_{s,e}'$ were first fully removed. This expected behavior made discerning the $T_{SWS,PP}$ and P_S straightforward, as these were considered to be respectively the SWS and PP magnitudes at the point of stabilization (indicated by arrows in Figure 8). The $T_{SWS,PP}$ values were within a range of 1.7–2.8 min (Table 3). Also, the T_{SWS} validation values found from the Sk method, $T_{SWS,Sk}$, showed good agreement with $T_{SWS,PP}$ (values in Table 3 and see Figure S5 for an analysis example). The discerned P_S timescale magnitudes ranged between 4.4 and 6.1 min for the HRS set (Table 3).

In order to discern P_S from PP for the LRS set, the same approach used for the HRS set was generally applicable for the lower stress tests (Figure 9b) but to a lesser degree for the higher stress tests. In fact, the PP behavior for the higher stress tests at $\langle \tau_{o,ap} \rangle^*/\tau_{cr}^* = 2.8$ and 3.2 was unexpected (Figures 9c–9d). For these tests, the PP exhibited cyclical peaks, which presented a key interpretation challenge (i.e., Figures 9c–9d). This PP behavior may be explained, however, when considering the influence of the bedload feeding period on exiting bedload that is described in Figure 7. Considering a feeding period of 2.5 and 2 min, respectively, for the $\langle \tau_{o,ap} \rangle^*/\tau_{cr}^* = 2.8$ and 3.2 cases, the influence of the bedload feeding period was effectively removed and distinct PP peaks (indicated with the blue circles in Figure 9) were visually identified as being regularly

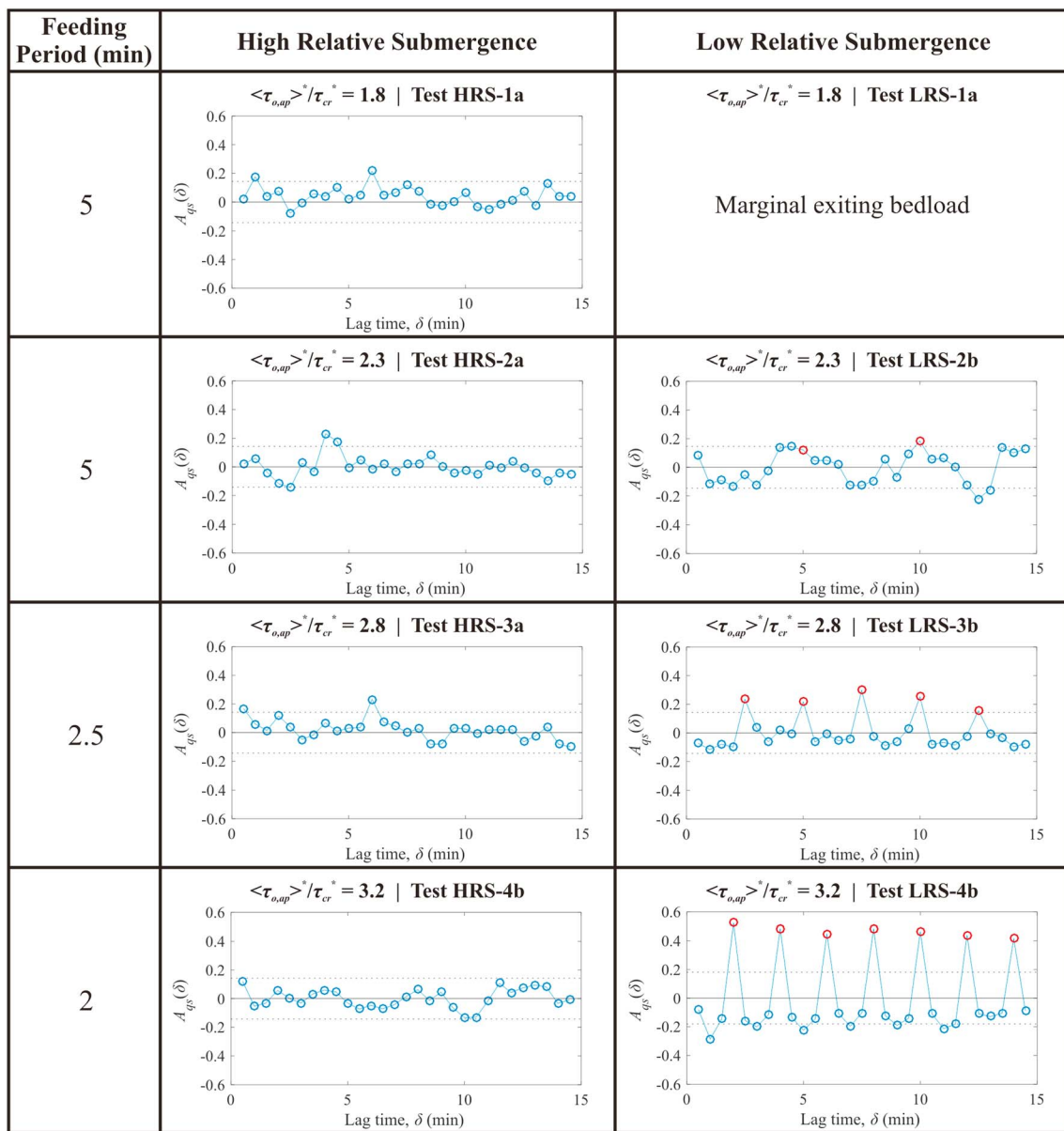


Figure 7. Autocorrelation, $A_{qs}(\delta)$, of the 30-s sampled $q_{s,e}$ time series for HRS and LRS tests selected from each tested flow condition; red points for the LRS tests correspond to lag times at multiples of the feeding period; statistical significance bounds at the 95% confidence interval are given by black dotted lines. HRS = High Relative Submergence; LRS = Low Relative Submergence.

spaced near exact multiples of the bedload feeding period. The discerned P_S timescales fall in a range of 4.2–5.3 min for the LRS set, which are comparable to the HRS set values (Table 3).

Examining the trends in P_S for the present experiments, a statistically significant negative correlation ($p = 0.05$) with $\langle \tau_{gr} \rangle^*$ was observed for the LRS set ($R^2 = 0.92$) but not for the HRS set (Figure S6). The wider variability in P_S magnitudes between test replicates in the HRS set was a key factor affecting possible trend conclusions for this data set. The overall P_S timescale magnitudes determined herein are at the low end of the 6–18 min magnitude range reported by Cudden and Hoey (2003), who used the PP method to determined P_S values (labeled the dominant period in their work) for bedload time series taken in natural gravel-bed rivers. Cudden and Hoey (2003) attributed bedload fluctuations in their study primarily to the effects of low-amplitude migrating bedforms. In the present experiments, the authors suggest that P_S reflects the effects the boulder array has on particle migration downstream (more detail is provided in section 4).

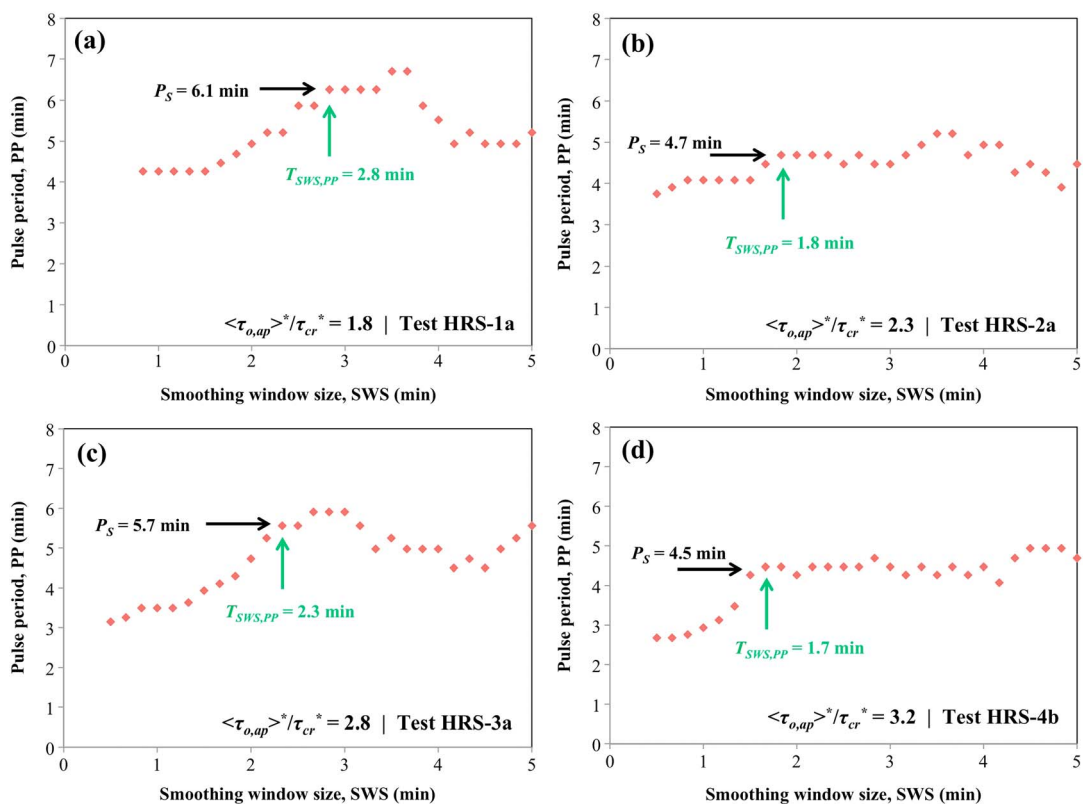


Figure 8. Determination of P_S for HRS tests selected from each tested flow condition by using the PP presented as a function of the moving average SWS. (a) Test HRS-1a; (b) test HRS-2a; (c) test HRS-3a; and (d) test HRS-4b. The threshold SWS values determined from the PP method, $T_{SWS,PP}$, are indicated with green arrows. HRS = High Relative Submergence; SWS = smoothing window size; PP = pulse period; P_S = small-scale periodicity.

Boulders and the depositional patches around them reduce the available space for conveyance and thus individual particles may tend to agglomerate as they exit the array, thereby mimicking the effects of congested zones on bedload pulsation (e.g., Iseya & Ikeda, 1987).

3.3.3. Large-Scale Periodicity, P_L

P_L in the exiting bedload time series, $q_{s,e}'$, is identified when smoothing $q_{s,e}'$ using SWS equated to P_S . The smoothed time series, shown in Figures 10a and 11a, highlight the fluctuations about the average bedload rate that occurred with relatively large timescales (about 10–40 min) for the selected HRS and LRS tests, respectively. To isolate the P_L magnitude, the temporal correlation characteristics of each smoothed time series were investigated through $A_{qs}(\delta)$, which are presented in Figures 10b and 11b for the HRS and LRS tests, respectively. In each $A_{qs}(\delta)$ plot, the first peak exceeding the 95% confidence threshold (indicated by red circles) was considered to represent the P_L timescale magnitude. The P_L magnitudes discerned from this analysis ranged from 12 to 46 min for the HRS tests and from 8 to 25 min for the LRS tests and generally decreased in magnitude with increasing bed shear stress (Table 3).

The authors suggest herein that bedload fluctuations at the P_L timescale are connected with large bedload releases around boulders. Therefore, the potential connection of P_L with the hydrodynamic influences of boulders on bedload deposition and mobilization in their vicinity is investigated through timescale normalization (e.g., Jain, 1992). Thus, the timescales for large bedload fluctuations, T_{bl} , are expressed in a dimensionless form, T^* , as follows:

$$T^* = \frac{T_{bl}}{T_{hyd}}, \quad (6)$$

where T_{hyd} is a characteristic hydrodynamic timescale that considers the influences of vortex shedding around boulders on bedload transport. An inherent assumption herein is that the time period, T^* , between

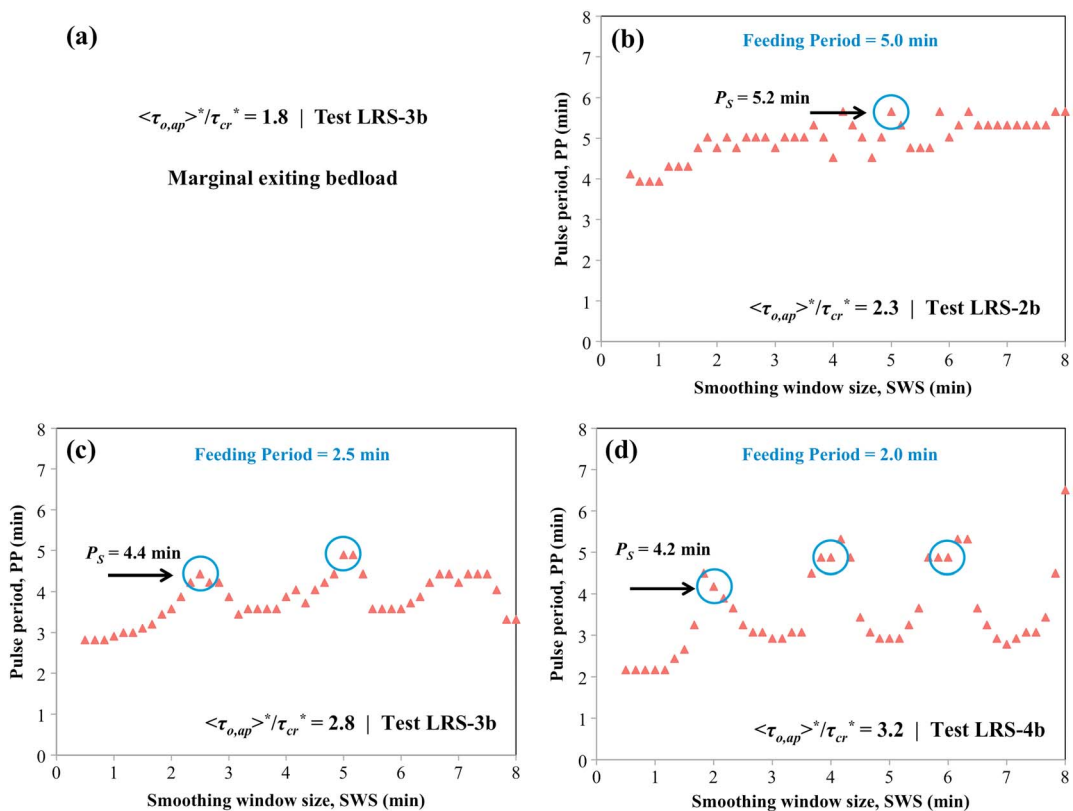


Figure 9. Determination of P_S for LRS tests selected from each tested flow condition by using the PP presented as a function of the moving average SWS. (a) Test LRS-1b; (b) test LRS-2b; (c) test LRS-3b; and (d) test LRS-4b. Multiples of the feeding period are circled in blue. LRS = Low Relative Submergence; SWS = smoothing window size; PP = pulse period; P_S = small-scale periodicity.

sequential large-scale releases or fluctuations for both HRS and LRS conditions is controlled by the magnitude and timescale of flow structures around boulders (i.e., in the wake, stoss, and flanks). Systematic variability of the magnitude, scale, and timing of these flow structures affects the capacity of boulders to offer further protection to existing deposited particles and also provide shelter to incoming particles. T_{hyd} in equation (6) is therefore defined as the timescale of the oscillatory nature of boulder eddies, T_{BE} :

$$T_{hyd} = T_{BE} = \frac{d_c}{St \times U_{d_c}}, \quad (7)$$

where St denotes the dimensionless Strouhal number; it is recalled also that d_c denotes the boulder diameter and U_{d_c} denotes the boulder approach velocity averaged over the boulder height. A review of reported studies with flow and obstacle characteristics that are most similar to those herein yielded a range of $St = 0.14\text{--}0.24$ for the wake structures and $St = 0.17\text{--}0.3$ for the stoss structures such as the HSV (Ettema et al., 2006; Hajimirzaie et al., 2014; Hajimirzaie & Buchholz, 2013; Lacey & Rennie, 2012; Okamoto, 1982; Paik et al., 2007). Therefore, the commonly used value of $St = 0.20$ was considered hereafter to estimate T_{BE} .

In order to validate the P_L trends found in the present study, comparisons with findings reported in the literature for bedload fluctuation timescales conducted for both with and without boulders are performed. A key comparison is with the study of Ghilardi et al. (2014b), who reported bedload fluctuation timescales from companion experiments both with and without a boulder array. In addition, bedload fluctuation timescales that were primarily associated with bedload sheets were compiled from Kuhnle and Southard (1988), Bennett and Bridge (1995), Nelson et al. (2009), and Recking et al. (2009). Timescales associated with the average period between the breakup of particle clusters were also taken from Strom et al. (2004). It was assumed that clusters had a similar impact to that of boulders by contributing pulses of sediment during consecutive cycles of formation and breakup.

Table 3

Timescales in Bedload Transport Exiting the Boulder Array

Experimental set	Test	Reach-averaged, dimensionless, normalized approach $\langle \tau_{o,ap} \rangle^*/\tau_{cr}$ (–)	Bedload feeding period (min)	Threshold smoothing window size, T_{SWS} (min)		Small-scale periodicity, P_S (min)	Large-scale periodicity, P_L (min)
				$T_{SWS,Sk}$ (min)	$T_{SWS,PP}$ (min)		
HRS	1a	1.84	5.0	1.8	2.8	6.1	40.2
	1b			2.3	2.3	5.2	15.3
	2a	2.30	5.0	2.8	1.8	4.7	32.2
	2b			1.8	2.2	4.7	46.0
	3a	2.76	2.5	2.5	2.3	5.7	31.3
	3b			2.3	2.3	4.4	20.2
	4a	3.22	2.0	2.7	2.7	4.9	12.3
	4b			2.5	1.7	4.5	13.5
LRS	1a	1.84	5.0	<i>Marginal exiting bedload</i>			
	1b			<i>Method not applicable because of feeding period influence</i>		5.3	25.0
	2a	2.30	5.0			5.2	24.5
	2b					NA ^a	NA ^a
	3a	2.76	2.5			4.4	19.5
	3b					4.5	8.0
	4a	3.22	2.0			4.2	13.7
	4b						

Note. Sk = skewness; PP = pulse period; HRS = High Relative Submergence; LRS = Low Relative Submergence.

^aThis test replicate excluded because of error in the experimental duration.

For the data set in the presence of boulders from Ghilardi et al. (2014b), T_{BE} was employed as T_{hyd} similarly to the present experiments (see Appendix B for assumptions concerning U_{dc}). For the studies conducted in the absence of boulders, however, T_{hyd} was selected as the timescale associated with large-scale eddies atop a flat rough bed, T_{LSE} . This timescale considers the outer flow variables (Cantwell, 1981), U_{bulk} and flow depth, as well as the role of the aspect ratio since large-scale flow structures tend to scale with the channel width (Dinehart, 1999). T_{LSE} was calculated as

$$T_{hyd} = T_{LSE} = 5.7 \frac{H}{U_{bulk}} \left(\frac{B}{H} \right)^{0.6}, \quad (8)$$

by using the parameterization proposed by Cameron et al. (2017) and considering an eddy convective velocity equal to U_{bulk} . The compiled bedload timescales with the predescribed T^* normalization are presented as a function of the reach-averaged, excess normalized grain shear stress, $\langle \tau_{gr} \rangle^*/\tau_{cr} - 1$, in Figure 12. The filled shapes correspond to the data with boulders and the hollow shapes to data without boulders, which are associated with bedload sheets and cluster breakup. In general, the T^* values from all data decrease as the ratio $\langle \tau_{gr} \rangle^*/\tau_{cr} - 1$ increases, except for the flatter trend exhibited for conditions very near τ_{cr} (i.e., tests with $\langle \tau_{gr} \rangle^*/\tau_{cr} - 1$ less than about 0.2). The decreasing trend at higher shear stresses indicates overall that the frequency of bedload fluctuations increases at higher flow conditions, which agrees with findings from previous researchers (e.g., Ghilardi et al., 2014b; Kuhnle & Southard, 1988). Investigating the data from the experiments with boulders (filled shapes), a close collapse is seen between the present study and that of Ghilardi et al. (2014b) within the range of $\langle \tau_{gr} \rangle^*/\tau_{cr} - 1$ greater than 0.2. This agreement is present despite the fact that the P_L values in this study are more than an order of magnitude less than some of the timescales reported by Ghilardi et al. (2014b) at similar $\langle \tau_{gr} \rangle^*/\tau_{cr} - 1$. Within the range of $\langle \tau_{gr} \rangle^*/\tau_{cr} - 1$ less than 0.2 and in the presence of boulders, it is not possible to directly compare the two studies since the data from Ghilardi et al. (2014b) do not extend to these conditions. Considering next the data without boulders (hollow shapes), it is shown that the data follow a similar trend and band of scatter as the data with boulders, but that there are greater differences between individual studies. These differences are likely attributed to the influences of grain sorting on bedload fluctuations in these experiments (e.g., Seminara et al., 1996), which are not accounted for in Figure 12.

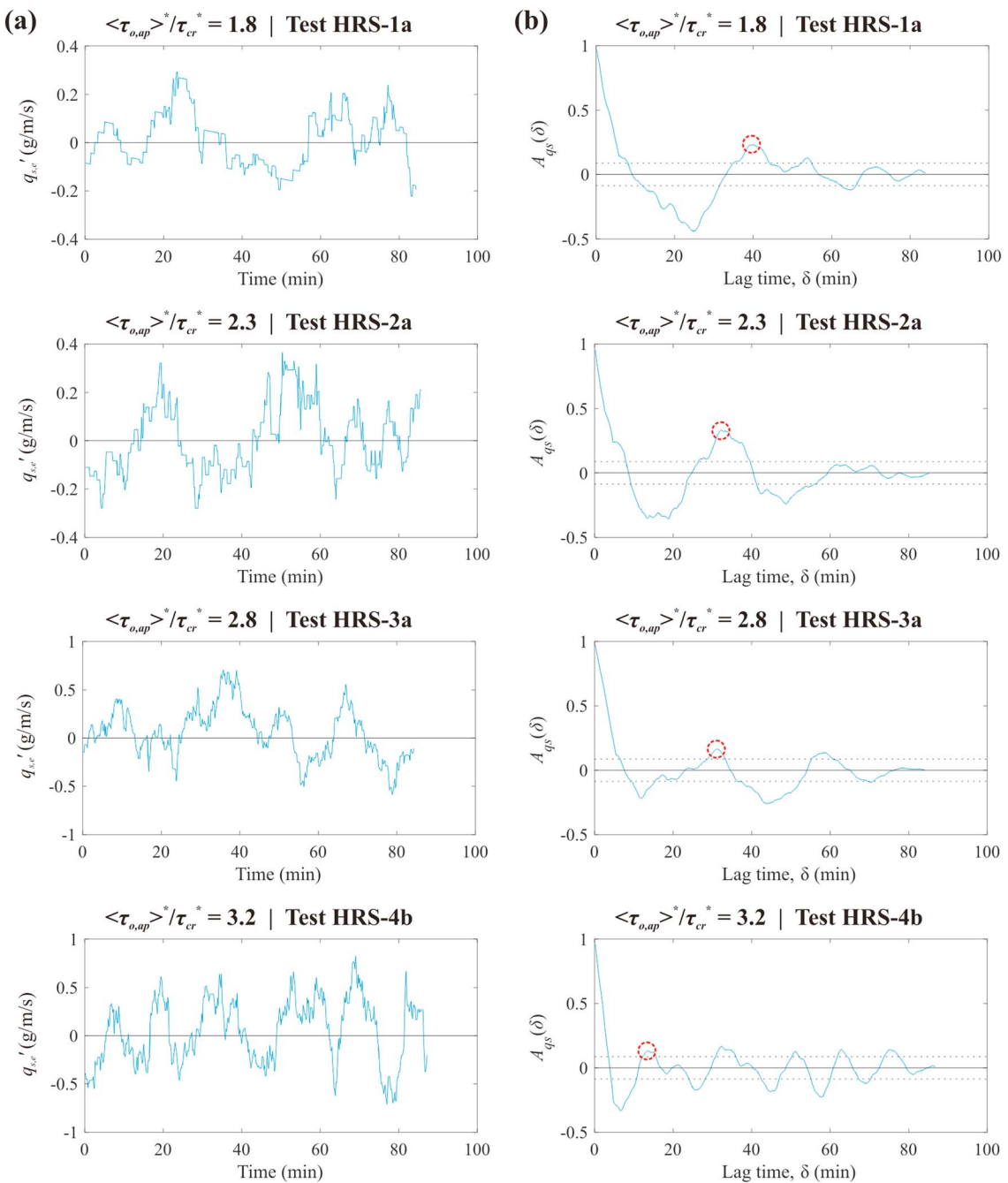


Figure 10. Determination of the large-scale periodicity for HRS tests selected from each tested flow condition. (a) The $q_{s,e}'$ time series smoothed with the small-scale periodicity; and (b) corresponding autocorrelation, $A_{qs}(\delta)$, plots where the large-scale periodicity is indicated with red circles. HRS = High Relative Submergence.

To affirm that T_{BE} is the appropriate T_{hyd} choice for bedload fluctuations in the presence of boulders, T_{BE} and T_{LSE} were compared for these experiments. For the present tests, T_{BE}/T_{LSE} was equal to 0.16 ± 0.001 and 0.29 ± 0.03 for the HRS and LRS experimental sets, respectively. This shows that approximately an order of magnitude drop in T^* and a decrease in collapse between the HRS and LRS sets would result from normalizing T_{bl} with T_{LSE} in place of T_{BE} . Interestingly, T_{BE}/T_{LSE} was near unity for the experiments of Ghilardi et al. (2014b), being equal to 0.99 ± 0.23 . This behavior is likely attributed to the reduced relative protrusion of the boulders in the Ghilardi et al. (2014b) experiments.

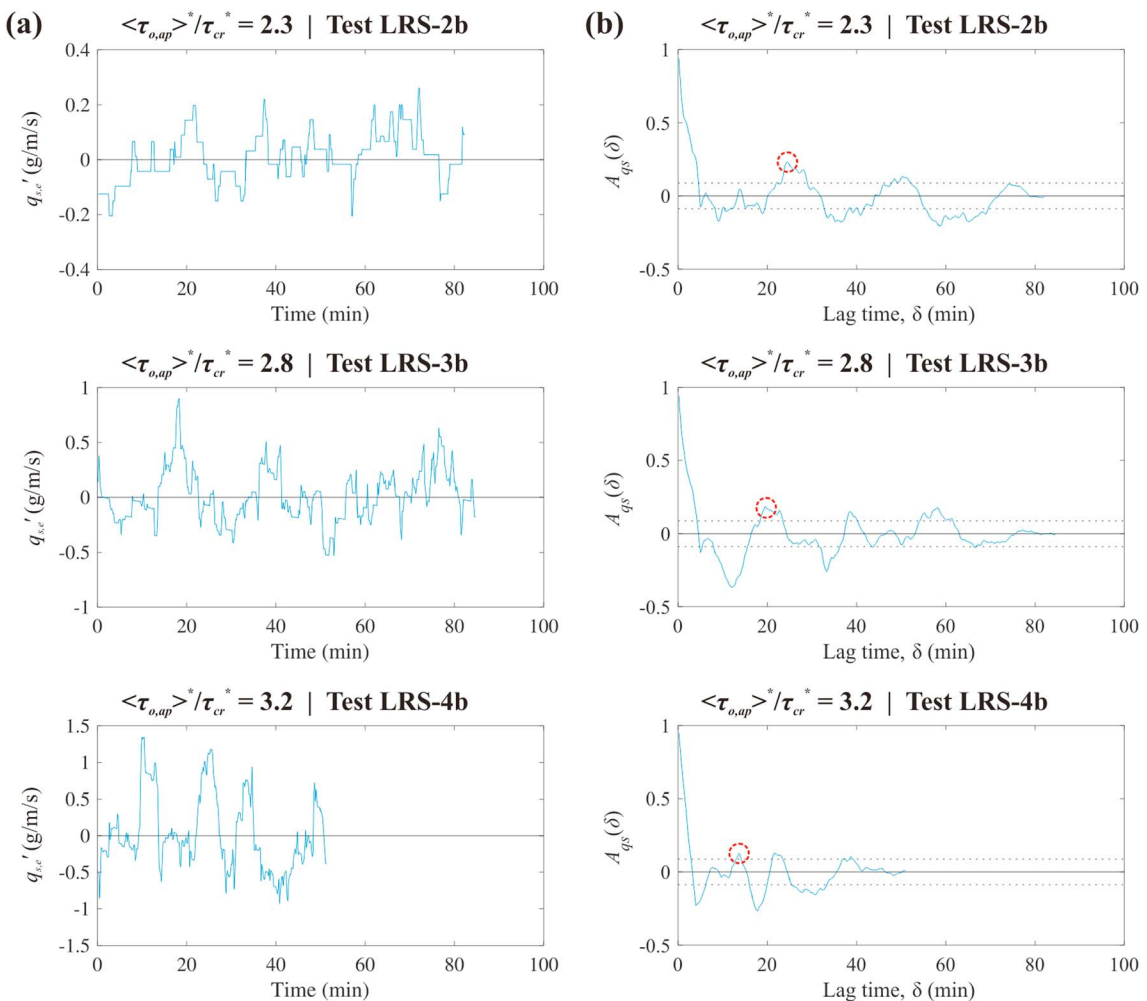


Figure 11. Determination of the large-scale periodicity for LRS tests selected from each tested flow condition. (a) The $q_{s,e}'$ time series smoothed with the small-scale periodicity; and (b) corresponding autocorrelation, $A_{qs}(\delta)$, plots where the large-scale periodicity is indicated with red circles. LRS = Low Relative Submergence.

4. Discussion

In the following subsections, the implications of these results are discussed regarding (1) the role of relative submergence and Froude number on bedload within the boulder array and (2) the connections between bedload timescales and boulder controls on bedload transport.

4.1. Key Hydraulic Parameters and Boulder Effects on Bedload

The boulder relative submergence has been highlighted herein as a key hydraulic parameter influencing the effects of a boulder array on bedload transport. While this parameter has been investigated in past research to show the implications to the surrounding flow field (e.g., Lacey & Rennie, 2012; Papanicolaou & Tsakiris, 2017; Shamloo et al., 2001), its effects on bedload transport rates, including pulsation, have been examined only in a rather qualitative fashion. Few studies have isolated the sole role of boulders on bedload releases as function of the excess shear stress while considering stress partitioning due to boulders bearing a fraction of the available total stress (Papanicolaou et al., 2011; Yager et al., 2007). This research although limited in terms of particle shape complexity (i.e., spheres are used) and bed configuration (i.e., bed is flat and well-packed) provides the means for isolating pulses of bedload fluctuations triggered by the boulder releases using established statistical methods such as the PP and normalized autocorrelation functions.

The direct connection of the HRS and LRS conditions with reversed predominant depositional locations relative to individual boulders is another key observation from this study. Namely, deposition mostly

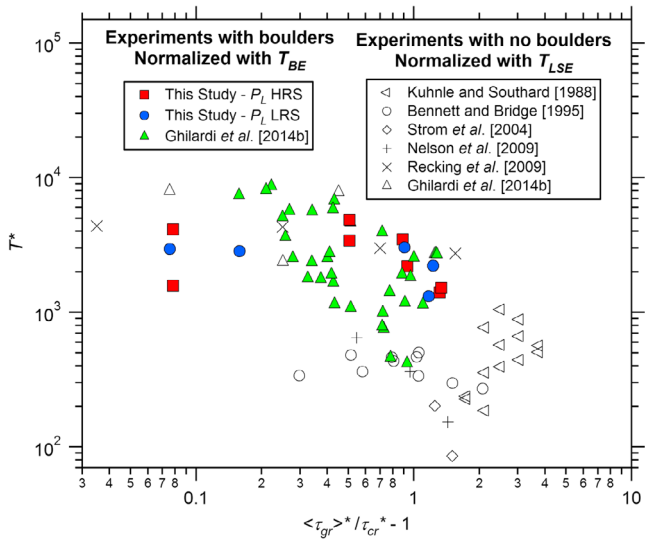


Figure 12. Normalized bedload fluctuation timescales, T^* , presented as a function of the reach-averaged, excess normalized grain shear stress, $\langle\tau_{gr}\rangle^*/\tau_{cr}^* - 1$. Timescales from experiments with boulders are normalized with the characteristic timescale of boulder eddies, T_{BE} . Timescales from experiments without boulders are normalized with the characteristic timescale of large-scale eddies atop a flat rough bed, T_{LSE} . Note: Total instead of grain shear stress is used for Ghilardi et al. (2014b) data due to lack of sufficient information for applying stress decomposition. P_L = large-scale periodicity; HRS = High Relative Submergence; LRS = Low Relative Submergence.

of the sediment deposition around a boulder but the effective area or characteristic length scale and frequency of the associated vortex topology (Papanicolaou et al., 2012).

Another topic that should be considered in future research is the potential role that surface-subsurface interactions in the vicinity of boulders can have to bedload transport. Within an identical boulder array to the present study, Uchida et al. (2016) have shown how the presence of boulders atop the porous, well-packed bed influences the formation of a vortex layer on the bed surface and a roughness layer under the bed surface (see Figure 1 in Uchida et al., 2016). Momentum exchanges between the two layers affect the pressure field near the bed with potential implications to particle segregation and mobilization, which should be investigated in future studies.

Future research should also investigate the depositional morphology within a boulder array at steady state bedload transport conditions (i.e., $\overline{q_{s,in}} = \overline{q_{s,e}}$). Such conditions were not considered here since these experiments were designed to only investigate the role of the array on bedload trapping and conveyance (i.e., Figure 6). If the present tests were replicated with longer duration to approach steady state conditions, it is expected that the array would entrap more total material within the depositional patches since $\overline{q_{s,trap}}$ was greater than zero at the end of the present tests (Figure 6b). However, the authors expect that similar patterns of local deposition would occur in both the shorter and longer experiments because local flow characteristics around boulders control depositional patterns.

In terms of bedload timing, a unique finding from this study is that $\langle H \rangle/d_c$ affected the diffusion of bedload supply timing signals through the boulder array. Bedload diffusion is defined by Nikora et al. (2002) as the scaling growth of the particle position statistics in time when viewed in the Lagrangian framework. From analysis of the Eulerian bedload time series, Figure 7 suggests that a portion of the supplied sediment was advected through the boulder array under LRS conditions. This advection was indicated by the coincidence of $A_{qs}(\delta)$ peaks with the bedload feeding period and the persistence of these peaks for higher time lag multiples. The absence of similar $A_{qs}(\delta)$ signatures for the HRS tests (Figure 7) suggests that bedload streamwise particle movement was more diffusive at HRS. Since the bedload feeding characteristics were similar for both HRS and LRS tests, this difference in exiting bedload behavior must

occurred in the wake of boulders at HRS and stoss of boulders at LRS (Figures 2, 3). Investigating the flow field characteristics around boulders, Papanicolaou and Tsakiris (2017) recently provided evidence that this reversal in depositional location corresponds with the distinct topologies of turbulent vortex structures that develop at HRS and LRS conditions. Specifically, at HRS conditions the vortex topology in the boulder wake is dominated by arch vortices, which induce circulation to promote the entrainment of bedload sediment in the boulder wake region (Papanicolaou & Tsakiris, 2017; Tsakiris, Papanicolaou, Hajimirzaie et al., 2014). In contrast, the limited available data at boulder LRS conditions suggest that in the case of $Fr < 1$ the necklace developed by the bimodal state of the HSV creates entrainment of sediment at the stoss; in the case of $Fr > 1$ it is the LWCs and potentially a von-Karman vortex street, which controls deposition and effective area of deposition (Papanicolaou et al., 2011; Shamloo et al., 2001). Research has further suggested that these different vortex structures in the boulder region under HRS and LRS conditions have different impacts on the bed shear stress directionality and magnitude (Monsalve & Yager, 2017; Papanicolaou et al., 2011; Papanicolaou & Tsakiris, 2017). Thus, $\langle H \rangle/d_c$ is believed to influence bedload depositional locations through its impacts on the local hydrodynamics and vortex topology developing around boulders. More research is needed, however, in linking the role of vortex topology with the effective area they create for sediment entrainment. This necessitates a change in paradigm. A recognition that it is not only the magnitude and directionality of the stress that affects the location

therefore be attributed to differences in transport characteristics between the HRS and LRS sets. Considering the HRS set observations, it is possible that the diffusive streamwise bedload movement is associated with the observed deposition along the flume sidewalls (i.e., Figure 2), since this indicates lateral bedload movement. This behavior was attributed previously to Prandtl's second kind secondary currents generated from the boulders presence and helps to explain the present results in part (Papanicolaou, 2012). Previous research on sediment pulse dynamics in the absence of boulders has also suggested that Fr may be a controlling parameter, with low Fr generally being linked to the translation, or advection, of an incoming pulse (e.g., Lisle et al., 1997, 2001; Sklar et al., 2009). This trend with Fr is not consistent for the present data in the presence of boulders, however, because bedload supply pulses were advected more in the LRS data set that also had the higher Fr values (Table 1). The present results therefore suggest that $\langle H \rangle/d_c$ is the key parameter influencing the diffusion of bedload movement in the presence of a boulder array. Overall, the authors hypothesize that this behavior is related to differences in flow structure within the boulder array at HRS and LRS conditions, though future research in flow structure interactions is needed to pinpoint the exact mechanisms. Future research must also connect the utility of a boulder array with stream restoration approaches for sediment flashiness. Depending on what is the objective of a restoration project the sizing of boulders must be viewed through the context of $\langle H \rangle/d_c$ for attaining advective or diffusive transport.

Fr was identified herein as the second key hydraulic parameter that influenced the effects of the boulder array on bedload. This parameter was predominantly important for the LRS test set, wherein a transition from subcritical to supercritical flow conditions occurred (Table 1) along with a corresponding change in the depositional location (Figure 3). The particular linkage between altered depositional features (Figures 4, 5) and surface wave structure differences in the subcritical and supercritical flow regimes has been similarly documented by Boyer and Roy (1991), though is not well researched in other literature. At present, the cause for the connection between LWCs around boulders and bedload deposition has not been explicitly made, but previous research from Chanson (2000) suggests that local near-bed hydrodynamics play a role. In particular, Chanson (2000) found that local minima in bed shear stress occurred under three dimensional standing wave crests in undular flow. It is hypothesized here that similar behavior occurred under LWCs and explains the observed connection with bedload deposition, though future studies are needed to further substantiate the claim made.

In order to predict mean bedload rates via stress decomposition, the importance of simultaneously considering $\langle H \rangle/d_c$ and Fr when selected C_d was emphasized herein, which was similarly highlighted by Flammer et al. (1970). While the effects of $\langle H \rangle/d_c$ on C_d are commonly considered when studying flow and sediment transport in the vicinity of boulders (e.g., Baki et al., 2014; Ferguson, 2007; Schneider et al., 2015), the effects of Fr have been minimally considered in these formulations. The present LRS results show an abrupt two-fold change in C_d when the flow transitions from subcritical to supercritical flow, highlighting the potential for significant errors in estimation of $\langle \tau_{gr} \rangle$, and subsequently of bedload transport rates, if the Fr effects are ignored.

4.2. Bedload Timescales and Connections With Boulder Controls

Past studies have investigated the intermittency of bedload especially at low shear stresses (e.g., Strom et al., 2004) and mostly in the absence of boulders. The recognition that the temporal structure of bedload transport within the boulder array is characterized by distinct timescales of fluctuation and the quantification of the timescale of bedload release exiting the array (e.g., Bacchi et al., 2014; Ghilardi et al., 2014a; Ma et al., 2014) are key contributions of this study. In the following, the cycles of bedload deposition and mobilization in the vicinity of boulders are discussed and viewed in concert to their likely connection with the observed P_L timescale.

In addition to the bedload time series analyses, side-view images and videos are herein utilized to reconfirm the cycles of bedload deposition and mobilization in the boulder vicinity. Two such side-view images are presented in Figure 13, which were selected from the HRS set in order to provide a clear case study illustration of a cycle of bedload deposition and mobilization in the vicinity of boulders. Figure 13a shows that boulders in the third row within the boulder array promoted the deposition of a notable amount of bedload material within the first 21 min following the commencement of test HRS-3b. Moreover, Figure 13b shows that a significant portion of the bedload material that deposited within the first 21 min of the test (Figure 13a)

$$\langle \tau_{o,ap} \rangle^*/\tau_{cr}^* = 2.8 \mid \text{Test HRS-3b}$$

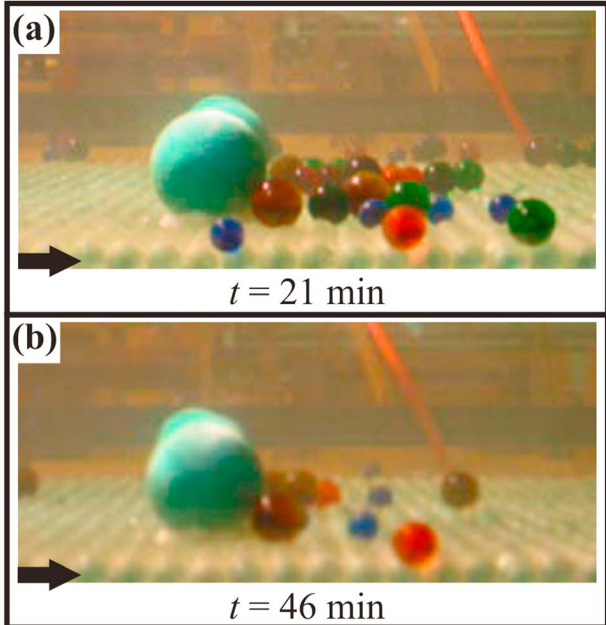


Figure 13. Side-view images showing changes in the number of particles stored in the wake region of a boulder for test HRS-3b. (a) Particles stored at $t = 21$ min into the test; and (b) particles stored at $t = 46$ min. Black arrows indicate flow direction. HRS = High Relative Submergence.

was mobilized within the following 25 min of the test. Thus, Figure 13 illustrates how boulders can generate fluctuations in bedload transport by promoting cycles of bedload deposition and mobilization in the wakes of boulders at HRS conditions. Within the LRS set, deposition and mobilization exchanges were also observed in the boulder vicinity (see Figures S7 and S8 and Text S1 for observations and descriptions of such exchanges), though the characteristics of exchanges differed because of the differences in depositional location that were overviewed in section 3.1.

The provided illustrations of bedload exchanges in the vicinity of boulders show the plausibility of authors' supposition that cycles of deposition and mobilization were responsible for generating P_L in the present experiments. Accordingly, it is hypothesized by the authors that a complex set of factors may influence the P_L timescale, including the characteristics of local hydrodynamics in the vicinity of boulders, the storage area available to temporarily harbor mobile bedload, and the interaction of boulders with incoming bedload material. Due to the limited availability of data to track temporal changes in bedload storage around individual boulders, however, a direct connection of the observed P_L fluctuations with the cycles of deposition and mobilization in the vicinity of boulders is not feasible at present in order to validate the proposed hypothesis. In addition, synchronous measurements of flow velocity and bedload movement in the boulder vicinity were not made as part of this research to allow explicit connections between bedload mobilization and flow structures developing around boulders. Future research is needed to address these limitations and to connect the observed bedload fluctuation timescales with their driving mechanisms.

5. Conclusions

This study has investigated the effects of a boulder array on the regulation of bedload transport through the use of laboratory experiments aiming to isolate the role of boulders. The primary findings from this study are summarized as follows:

1. Depositional patches of bedload material formed around individual boulders and characterized the local bed morphology in the present experiments. The predominant locations of depositional patches relative to individual boulders were separated into three distinct cases based on two key hydraulic parameters: (1) the boulder relative submergence, $\langle H \rangle/d_c$, which is defined as the ratio of the reach-averaged flow depth in the boulder array, $\langle H \rangle$, to the boulder or clast diameter, d_c , and (2) the Froude number, Fr . The Case 1 morphology occurred for all HRS tests (all with $Fr < 1$) and corresponded with deposition predominantly in boulder wake regions (Figure 2). On the contrary, deposition for all LRS tests occurred primarily on the upstream side of boulders and along their flanks (Figure 3). When $Fr < 1$ occurred at LRS, material deposited mostly in the stoss region upstream of individual boulders and is denoted here as the Case 2 morphology. However, when flow with $Fr > 1$ occurred at LRS, the Case 3 morphology occurred and bedload deposited under LWCs, which were located at the upstream flanks of individual boulders (Figure 4). This case delineation of bed morphological characteristics based on key hydraulic parameters ($\langle H \rangle/d_c$ and Fr) is an important contribution of this work. Moreover, connections with previous research suggests that $\langle H \rangle/d_c$ influences bed morphology through effects on the vortex topology around boulders (Papanicolaou & Tsakiris, 2017) and that Fr influences bed morphology through its effects on surface wave structure around boulders (Boyer & Roy, 1991).
2. Observations of depositional locations with respect to the boulder array reach also corresponded with the delineated cases of local morphology (Figures 2, 3). For the morphology in Cases 1 and 2, deposition occurred primarily toward the entrance of the boulder array. For the Case 3 morphology, however,

deposition occurred within the middle portion of the array (along the streamwise direction) and minimal bedload deposited in the first 4–6 boulder rows. Investigation of this behavior highlighted again the connection between LWCs and deposition at LRS with $Fr > 1$ because LWCs did not occur at the array entrance and were developed near the location of the first observed depositional patches (Figure 5).

3. The effects of the boulder array in regulating bedload transport rates were evaluated in terms of the mean exiting and trapping rates. Stress decomposition methods similar to Yager et al. (2007) were employed herein and shown to be effective in aiding prediction of these rates. However, the appropriate selection of the drag coefficient, C_d , was found to be particularly important for this data set and the fitted values varied between 0.70 and 1.73 for the range of examined conditions. Similar to the findings of Flammer et al. (1970), the present results emphasize the importance of simultaneously considering $\langle H \rangle / d_c$ and Fr when selecting C_d in order to estimate the stress borne by immobile boulders. Employing the estimated bed shear stress within the array, mean exiting bedload rates agreed closely with the data of Strom et al. (2004), who investigated bedload transport in the vicinity of stable particle clusters (Figure 6a). Furthermore, consideration of bedload continuity between the entrance and the exit of the boulder array revealed that the approach flow and array bed shear stress conditions can be used to describe closely the mean bedload trapping rates (Figure 6b).
4. The small-scale periodicity of bedload transport, P_S , was isolated in exiting bedload time series by the PP analysis (Cudden & Hoey, 2003) and fell within a narrow 4–6 min magnitude range (Figures 8, 9; Table 3). The authors suggest that P_S reflects the effects the boulder array has on particle migration downstream. Boulders and the depositional patches around them reduce the available space for conveyance and thus individual particles tend to agglomerate as they exit the array, thereby mimicking the effects of congested zones on bedload pulsation (e.g., Iseya & Ikeda, 1987). Future research is needed to confirm this hypothesis.
5. The large-scale periodicity of bedload transport, P_L , was discerned by the autocorrelation function, fell in the range of 8–46 min and generally decreased with increasing shear stress (Figures 10, 11 and Table 3). The authors suggest that bedload deposition and mobilization exchanges in the boulder vicinity are responsible for bedload rate fluctuations at the P_L timescale and that the timescale of these exchanges is connected with the influences of boulder eddies around them. This mechanism was illustrated in Figure 13 through a case study observing the bedload exchanges in the boulder wake region during an HRS test. In addition, the potential connection of P_L with the hydrodynamic influences of boulders on bedload deposition and mobilization in their vicinity was investigated through the normalization of P_L with the timescale of the oscillatory nature of boulder eddies, T_{BE} (Figure 12). This normalization approach may have significant implications for understanding bedload fluctuations in high-gradient gravel-bed rivers and warrants investigation in future studies.
6. Examining the timing of bedload transport, an interesting finding was that the timing signature of bedload feeding was reflected at the array exit for LRS conditions, but not for HRS conditions (Figure 7). This behavior suggests that bedload transport is more diffusive through the array at HRS and more advective at LRS. The control of other factors in the present experiments also indicates that $\langle H \rangle / d_c$ is the parameter most likely to explain this behavior. This finding may have significant implications for the timing of bedload conveyance through high gradient gravel-bed rivers, which often receive sporadic sediment inputs from steep landscapes.

The findings of this study overall support the interconnection of flow modification by the presence of immobile boulders and the role of boulders on bedload transport, which has been suggested in previous research (e.g., Monsalve & Yager, 2017; Papanicolaou & Tsakiris, 2017). These results can aid investigations of morphodynamic evolution in high gradient gravel-bed rivers by providing improved understanding of local bed morphology as well as of bedload entrapment and conveyance. In addition, the present results can help inform the time period used in the design of bedload sampling strategies for gravel-bed rivers, such as with acoustic geophone sensors (e.g., Tsakiris, Papanicolaou, & Lauth, 2014).

This research has built from previous studies that elucidated the effects of boulders on flow for a similar experimental setup and at comparable flow conditions (Papanicolaou et al., 2012; Papanicolaou & Tsakiris, 2017), and it has thus drawn important connections between bedload and expected flow field characteristics. A key component that is minimally understood in this body of research, however, is the effects that

surface-subsurface flow interactions around boulders can have on the near-bed flow field (e.g., Uchida et al., 2016) and how these modifications can affect bedload transport. Future research is needed to address this limitation and to better describe overall the local characteristics of bedload movement within a boulder array.

Appendix A: Estimating the Flow Adjustment Length Within the Array

The length scale describing the flow adjustment to the drag from the boulder array (or roughness canopy), L_c , is defined as (Belcher et al., 2003)

$$L_c = \frac{2(1 - \phi)}{C_d a}, \quad (A1)$$

where ϕ is the solid volume fraction occupied by boulders within the canopy (which extends in the vertical direction from the bed surface to the top of the boulders), C_d is the boulder drag coefficient, and a is the boulder frontal area per unit canopy volume. C_d was estimated in this study for three representative groups of experimental flow conditions: (1) HRS, (2) LRS with Froude number, $Fr < 1$, and (3) LRS with $Fr > 1$ (see section 2.1). For these three groups of conditions, C_d was estimated to be equal to 0.70, 1.73, and 0.84, respectively. Using equation (A1) with these C_d values, L_c is estimated for the three groups of conditions to be equal to 2.6, 1.1, and 2.3 m, respectively. These estimates suggest that the flow may be expected to exhibit transitioning flow characteristics for the upstream 21–50% of the total array length for the tested flow conditions.

Appendix B: Estimating Boulder Approach Velocity, U_{d_c}

The approach velocity to a boulder within the array, U_{d_c} , is defined as the average velocity across depths between the bed elevation and the boulder crest elevation. For tests with partially submerged boulders, it was assumed that $U_{d_c} = U_{RA}$, where U_{RA} is the reach-averaged velocity calculated as

$$U_{RA} = \frac{qw}{\left(\frac{2V_w}{\sqrt{3}\lambda}\right)}, \quad (B1)$$

where q is the discharge per unit width, w is the channel width, V_w is the total water volume (the reader is referred to Yager et al., 2007), and λ is the average boulder spacing (Yager et al., 2007). For tests with fully submerged boulders, U_{RA} is expected to be larger than U_{d_c} . For the HRS experiments herein, a velocity profile taken by the authors at the $\langle\tau_{o,ap}\rangle^*/\tau_{cr}^* = 2.3$ condition near a boulder at the centerline of the flume (Papanicolaou et al., 2012) was integrated to determine U_{d_c} for this condition. This yielded a ratio of $U_{d_c}/U_{RA} = 0.619$, which has been assumed valid for the rest of the HRS data set.

Analysis of data from Ghilardi et al. (2014b) has also required estimates of U_{d_c} . For experiments corresponding to partially submerged boulders, equation (B1) was used. At submerged conditions, the inflectional velocity profile proposed by Katul et al. (2002) was assumed valid because it was developed for use in the vicinity of large roughness elements and its form has been observed in studies within boulder arrays (Baki et al., 2016; Papanicolaou et al., 2012). Using the assumptions recommended by Katul et al. (2002) for gravel-bed rivers, the reference velocity was fitted to satisfy equality of the profile depth averaged velocity with U_{RA} . Finally, U_{d_c} was found by profile integration over the boulder height.

Appendix C: Fitting the Drag Coefficient, C_d , for Immobile Boulders

As derived by Yager et al. (2007), the flow discharge per unit width, q , required to achieve a certain average flow depth within a boulder array is calculated as

$$q = \sqrt{\frac{8gS_0 V_w^3}{3\lambda^2 w^2 (A_{IF} C_d + A_m C_m)}}, \quad (C1)$$

where g is the acceleration due to gravity, S_0 is the bed slope, V_w is the total volume of water in a control volume, λ is the spacing of boulders, w is the channel width, A_{IF} is the frontal area of immobile boulders within the control volume, C_d is the drag coefficient for immobile boulders, A_m is the bed area available to transport

mobile sediment (calculated by subtracting the bed parallel area of immobile boulders, A_{IP} , from the total area, A_t), and C_m is a drag coefficient associated with the bed friction.

When calculating stress borne by immobile boulders, Yager et al. (2007) used the reach-averaged velocity, U_{RA} , in the drag force equation. Herein, U_{dc} is instead used because this is more consistent with commonly employed definitions of C_d . A modified equation for calculating the reach-averaged stress borne by immobile boulders, $\langle\tau_l\rangle$, is therefore expressed as:

$$\langle\tau_l\rangle = \frac{1}{2}\rho C_d U_{dc}^2 \frac{A_{IF}}{A_{IP}}, \quad (C2)$$

which is a modified version of equation (4) in the manuscript of Yager et al. (2007). To derive a revised equation for predicting q , a boulder approach velocity correction coefficient, C_{app} , is defined as

$$C_{app} = \frac{U_{dc}}{U_{RA}}. \quad (C3)$$

Combining equations (C2) and (C3) with the equations originally employed by Yager et al. (2007) to derive equation (C1), a revised equation is for calculating q is expressed as follows:

$$q = \sqrt{\frac{8gS_0 V_w^3}{3\lambda^2 w^2 (A_{IF} C_d C_{app}^2 + A_m C_m)}}, \quad (C4)$$

where the addition of C_{app}^2 accounts for the difference between U_{dc} and U_{RA} . An estimate of C_m is the final requirement for applying equation (C4) to the present experiments, and it was considered a function of grain relative submergence (Scheingross et al., 2013). Thus, reach-averaged uniform flow depth data at conditions replicating approach flow conditions to the boulder array was used to develop the following equation ($R^2 = 0.75$):

$$C_m = 0.0227 (\langle H_{ap} \rangle / d_{bed})^{-0.232} \quad (C5)$$

As an outcome from equations (C4) and (C5), the q required to achieve a given reach-averaged uniform depth within the array, $\langle H \rangle$, is predicted (using $\langle H \rangle$ instead of $\langle H_{ap} \rangle$ in equation (C5)). Since all other variables are known or appropriately defined, C_d is fitted in order to minimize prediction errors of q .

Acknowledgments

The authors acknowledge the funding provided by the United States Geological Survey (USGS) Program 104 under Contracts 02HQGR0139 and 2017TN133B and by the United States National Science Foundation (NSF) under Award 1419073. Also, one of the coauthors (M.A.W.) was supported by the Chancellor's Fellowship awarded by the University of Tennessee at Knoxville. All data used in the manuscript are reported in the tables, figures, and supporting information. The authors would like to thank Angel Monsalve and two other anonymous reviewers for their insightful comments that helped enhance the overall quality of the manuscript.

References

- Bacchi, V., Recking, A., Eckert, N., Frey, P., Piton, G., & Naaim, M. (2014). The effects of kinetic sorting on sediment mobility on steep slopes. *Earth Surface Processes and Landforms*, 39(8), 1075–1086. <https://doi.org/10.1002/esp.3564>
- Baki, A. B. M., Zhang, W., Zhu, D. Z., & Rajaratnam, N. (2016). Flow structures in the vicinity of a submerged boulder within a boulder array. *Journal of Hydraulic Engineering*, 143(5), 04016031. [https://doi.org/10.1061/\(ASCE\)HY.1943-7900.0001273](https://doi.org/10.1061/(ASCE)HY.1943-7900.0001273)
- Baki, A. B. M., Zhu, D. Z., & Rajaratnam, N. (2014). Mean flow characteristics in a rock-ramp-type fish pass. *Journal of Hydraulic Engineering*, 140(2), 156–168. [https://doi.org/10.1061/\(ASCE\)HY.1943-7900.0000816](https://doi.org/10.1061/(ASCE)HY.1943-7900.0000816)
- Bathurst, J. C. (1987). Critical conditions for bed material movement in steep, boulder-bed streams. In R. L. Beschta, T. Blinn, G. E. Grant, F. J. Swanson, & G. G. Ice (Eds.), *Proc. Corvallis Symp. "Erosion and sedimentation in the Pacific Rim"*, (pp. 309–318). Wallingford, UK: IAHS Press.
- Belcher, S. E., Jerram, N., & Hunt, J. C. R. (2003). Adjustment of a turbulent boundary layer to a canopy of roughness elements. *Journal of Fluid Mechanics*, 488, 369–398. <https://doi.org/10.1017/S0022112003005019>
- Bennett, S. J., & Bridge, J. S. (1995). The geometry and dynamics of low-relief bed forms in heterogeneous sediment in a laboratory channel, and their relationship to water flow and sediment transport. *Journal of Sedimentary Research*, 65A(1), 29–39. <https://doi.org/10.1306/D4268013-2B26-11D7-8648000102C1865D>
- Bettess, R. (1984). Initiation of sediment transport in gravel streams. *Proceeding of the Institution of Civil Engineers*, 77(1), 79–88. <https://doi.org/10.1680/iicep.1984.1275>
- Boyer, C., & Roy, A. G. (1991). Morphologie du lit autour d'un obstacle soumis à un écoulement en couche mince. *Géographie Physique et Quaternaire*, 45(1), 91–99. <https://doi.org/10.7202/032848ar>
- Brayshaw, A. C. (1984). Characteristics and origin of cluster bedforms in coarse-grained alluvial channels. In E. H. Koster, & R. J. Steel (Eds.), *Sedimentology of gravels and conglomerates*, (pp. 77–85). Calgary, Alberta, Canada: Canadian Society of Petroleum Geologists.
- Buffington, J. M., & Montgomery, D. R. (1997). A systematic analysis of eight decades of incipient motion studies, with special reference to gravel-bedded rivers. *Water Resources Research*, 33(8), 1993–2029. <https://doi.org/10.1029/96WR03190>

- Bunte, K., & Poesen, J. (1993). Effects of rock fragment covers on erosion and transport of noncohesive sediment by shallow overland flow. *Water Resources Research*, 29(5), 1415–1424. <https://doi.org/10.1029/92WR02706>
- Byrd, T. C., Furbish, D. J., & Warburton, J. (2000). Estimating depth-averaged velocities in rough channels. *Earth Surface Processes and Landforms*, 25(2), 167–173. [https://doi.org/10.1002/\(SICI\)1096-9837\(200002\)25:2<167::AID-ESP66>3.0.CO;2-G](https://doi.org/10.1002/(SICI)1096-9837(200002)25:2<167::AID-ESP66>3.0.CO;2-G)
- Cameron, S. M., Nikora, V., & Stewart, M. (2017). Very-large-scale motions in rough-bed open-channel flow. *Journal of Fluid Mechanics*, 814, 416–429. <https://doi.org/10.1017/jfm.2017.24>
- Canovaro, F., Paris, E., & Solaro, L. (2007). Effects of macro-scale bed roughness geometry on flow resistance. *Water Resources Research*, 43, W10414. <https://doi.org/10.1029/2006WR005727>
- Cantwell, B. J. (1981). Organized motion in turbulent flow. *Annual Review of Fluid Mechanics*, 13(1), 457–515. <https://doi.org/10.1146/annurev.fl.13.010181.000235>
- Chanson, H. (2000). Boundary shear stress measurements in undular flows: Application to standing wave bed forms. *Water Resources Research*, 36(10), 3063–3076. <https://doi.org/10.1029/2000WR900154>
- Coleman, N. L. (1967). A theoretical and experimental study of drag and lift forces acting on a sphere resting on a hypothetical streambed. Paper presented at 12th Congress Int. Assoc. Hyd. Res., Fort Collins, CO.
- Cooper, J. R., Ockleford, A., Rice, S. P., & Powell, D. M. (2018). Does the permeability of gravel river beds affect near-bed hydrodynamics? *Earth Surface Processes and Landforms*, 43, 943–955. <https://doi.org/10.1002/esp.4260>
- Cryer, J. D., & Chan, K.-S. (2008). *Time series analysis: With applications in R*, (2nd ed.). New York: Springer-Verlag. <https://doi.org/10.1007/978-0-387-75959-3>
- Cudden, J. R., & Hoey, T. B. (2003). The causes of bedload pulses in a gravel channel: The implications of bedload grain-size distributions. *Earth Surface Processes and Landforms*, 28(13), 1411–1428. <https://doi.org/10.1002/esp.521>
- Dey, S., Sarkar, S., & Solaro, L. (2011). Near-bed turbulence characteristics at the entrainment threshold of sediment beds. *Journal of Hydraulic Engineering*, 137(9), 945–958. [https://doi.org/10.1061/\(ASCE\)HY.1943-7900.0000396](https://doi.org/10.1061/(ASCE)HY.1943-7900.0000396)
- Dinehart, R. L. (1999). Correlative velocity fluctuations over a gravel river bed. *Water Resources Research*, 35(2), 569–582. <https://doi.org/10.1029/1998WR900038>
- Diplas, P. (1987). Bedload transport in gravel-bed streams. *Journal of Hydraulic Engineering*, 113(3), 277–292. [https://doi.org/10.1061/\(ASCE\)0733-9429\(1987\)113:3\(277\)](https://doi.org/10.1061/(ASCE)0733-9429(1987)113:3(277))
- Elhakeem, M., Papanicolaou, A. N., & Tsakiris, A. G. (2016). A probabilistic model for sediment entrainment: The role of bed irregularity. *International Journal of Sediment Research*, 32(2), 137–148. <https://doi.org/10.1016/j.ijsrc.2016.11.001>
- Ettema, R., Kirkil, G., & Muste, M. (2006). Similitude of large-scale turbulence in experiments on local scour at cylinders. *Journal of Hydraulic Engineering*, 132(1), 33–40. [https://doi.org/10.1061/\(ASCE\)0733-9429\(2006\)132:1\(33\)](https://doi.org/10.1061/(ASCE)0733-9429(2006)132:1(33))
- Fenton, J. D., & Abbott, J. E. (1977). Initial movement of grains on a stream bed: The effect of relative protrusion. *Proceedings of the Royal Society A*, 352, 523–537. <https://doi.org/10.1098/rspa.1977.0014>
- Ferguson, R. (2007). Flow resistance equations for gravel- and boulder-bed streams. *Water Resources Research*, 43, W05427. <https://doi.org/10.1029/2006WR005422>
- Flammer, G. H., Tullis, J. P., & Mason, E. S. (1970). Free surface, velocity gradient flow past hemisphere. *Journal of the Hydraulics Division*, 96(7), 1485–1502.
- Fox, J. F., Papanicolaou, A. N., & Kjos, L. (2005). Eddy taxonomy methodology around a submerged barb obstacle within a fixed rough bed. *Journal of Engineering Mechanics*, 131(10), 1082–1101. [https://doi.org/10.1061/\(ASCE\)0733-9399\(2005\)131:10\(1082\)](https://doi.org/10.1061/(ASCE)0733-9399(2005)131:10(1082))
- Ghilardi, T., Franca, M. J., & Schleiss, A. J. (2014a). Bed load fluctuations in a steep channel. *Water Resources Research*, 50, 6557–6576. <https://doi.org/10.1002/2013WR014449>
- Ghilardi, T., Franca, M. J., & Schleiss, A. J. (2014b). Period and amplitude of bedload pulses in a macro-rough channel. *Geomorphology*, 221, 95–103. <https://doi.org/10.1016/j.geomorph.2014.06.006>
- Hajimirzaie, S. M., & Buchholz, J. H. J. (2013). Flow dynamics in the wakes of low-aspect-ratio wall-mounted obstacles. *Experiments in Fluids*, 54(11), 1616. <https://doi.org/10.1007/s00348-013-1616-1>
- Hajimirzaie, S. M., Tsakiris, A. G., Buchholz, J. H. J., & Papanicolaou, A. N. (2014). Flow characteristics around a wall-mounted spherical obstacle in a thin boundary layer. *Experiments in Fluids*, 55(6), 1–14. <https://doi.org/10.1007/s00348-014-1762-0>
- Hardy, R. J., Best, J. L., Lane, S. N., & Carboneau, P. E. (2009). Coherent flow structures in a depth-limited flow over a gravel surface: The role of near-bed turbulence and influence of Reynolds number. *Journal of Geophysical Research*, 114, F01003. <https://doi.org/10.1029/2007JF000970>
- Heays, K. G., Friedrich, H., & Melville, B. W. (2014). Laboratory study of gravel-bed cluster formation and disintegration. *Water Resources Research*, 50, 2227–2241. <https://doi.org/10.1002/2013WR014208>
- Hoey, T. B. (1992). Temporal variations in bedload transport rates and sediment storage in gravel-bed rivers. *Progress in Physical Geography*, 16(3), 319–338. <https://doi.org/10.1177/0309133392021600303>
- Iseya, F., & Ikeda, H. (1987). Pulsations in bedload transport rates induced by a longitudinal sediment sorting: A flume study using sand and gravel mixtures. *Geografiska Annaler: Series A*, 69, 15–27. <https://doi.org/10.1080/04353676.1987.11880193>
- Jain, S. C. (1992). Note on lag in bedload discharge. *Journal of Hydraulic Engineering*, 118(6), 904–917. [https://doi.org/10.1061/\(ASCE\)0733-9429\(1992\)118:6\(904\)](https://doi.org/10.1061/(ASCE)0733-9429(1992)118:6(904))
- Julien, P. Y., & Bounvilay, B. (2012). Velocity of rolling bed load particles. *Journal of Hydraulic Engineering*, 139(2), 177–186. [https://doi.org/10.1061/\(ASCE\)HY.1943-7900.0000657](https://doi.org/10.1061/(ASCE)HY.1943-7900.0000657)
- Katul, G., Wiberg, P., Albertson, J., & Hornberger, G. (2002). A mixing layer theory for flow resistance in shallow streams. *Water Resources Research*, 38(11), 1250. <https://doi.org/10.1029/2001WR000817>
- Knapp, D. D. (2002). Applications of particle velocity to bedload motion. M.S. thesis, Washington State University.
- Kuhnle, R. A., & Southard, J. B. (1988). Bed load transport fluctuations in a gravel bed laboratory channel. *Water Resources Research*, 24(2), 247–260. <https://doi.org/10.1029/WR024i002p00247>
- Lacey, R. J., & Rennie, C. D. (2012). Laboratory investigation of turbulent flow structure around a bed-mounted cube at multiple flow stages. *Journal of Hydraulic Engineering*, 138(1), 71–84. [https://doi.org/10.1061/\(ASCE\)HY.1943-7900.0000476](https://doi.org/10.1061/(ASCE)HY.1943-7900.0000476)
- Laronne, J. B., & Carson, M. A. (1976). Interrelationships between bed morphology and bed-material transport for a small, gravel-bed channel. *Sedimentology*, 23(1), 67–85. <https://doi.org/10.1111/j.1365-3091.1976.tb00039.x>
- Lenzi, M. A., Mao, L., & Comiti, F. (2006). When does bedload transport begin in steep boulder-bed streams? *Hydrological Processes*, 20(16), 3517–3533. <https://doi.org/10.1002/hyp.6168>
- Lisle, T. E., Cui, Y., Parker, G., Pizzuto, J. E., & Dodd, A. M. (2001). The dominance of dispersion in the evolution of bed material waves in gravel-bed rivers. *Earth Surface Processes and Landforms*, 26(13), 1409–1420. <https://doi.org/10.1002/esp.300>

- Lisle, T. E., Pizzuto, J. E., Ikeda, H., Iseya, F., & Kodama, Y. (1997). Evolution of a sediment wave in an experimental channel. *Water Resources Research*, 33(8), 1971–1981. <https://doi.org/10.1029/97WR01180>
- Ma, H., Heyman, J., Fu, X., Mettra, F., Ancey, C., & Parker, G. (2014). Bed load transport over a broad range of timescales: Determination of three regimes of fluctuations. *Journal of Geophysical Research: Earth Surface*, 119, 2653–2673. <https://doi.org/10.1002/2014JF003308>
- Monsalve, A., & Yager, E. M. (2017). Bed surface adjustments to spatially variable flow in low relative submergence regimes. *Water Resources Research*, 53, 9350–9367. <https://doi.org/10.1002/2017WR020845>
- Monsalve, A., Yager, E. M., Turowski, J. M., & Rickenmann, D. (2016). A probabilistic formulation of bed load transport to include spatial variability of flow and surface grain size distributions. *Water Resources Research*, 52, 3579–3598. <https://doi.org/10.1002/2015WR017694>
- Morris, H. M. (1955). Flow in rough conduits. *Transactions of the American Society of Civil Engineers*, 126, 373–398.
- Nelson, P. A., Venditti, J. G., Dietrich, W. E., Kirchner, J. W., Ikeda, H., Iseya, F., & Sklar, L. S. (2009). Response of bed surface patchiness to reductions in sediment supply. *Journal of Geophysical Research*, 114, F02005. <https://doi.org/10.1029/2008JF001144>
- Nikora, V., Gorling, D., McEwan, I., & Griffiths, G. (2001). Spatially averaged open-channel flow over rough bed. *Journal of Hydraulic Engineering*, 127(2), 123–133. [https://doi.org/10.1061/\(ASCE\)0733-9429\(2001\)127:2\(123\)](https://doi.org/10.1061/(ASCE)0733-9429(2001)127:2(123))
- Nikora, V., Habersack, H., Huber, T., & McEwan, I. (2002). On bed particle diffusion in gravel bed flows under weak bed load transport. *Water Resources Research*, 38(6), 1081. <https://doi.org/10.1029/2001WR000513>
- Nitsche, M., Rickenmann, D., Turowski, J. M., Badoux, A., & Kirchner, J. W. (2011). Evaluation of bedload transport predictions using flow resistance equations to account for macro-roughness in steep mountain streams. *Water Resources Research*, 47, W08513. <https://doi.org/10.1029/2011WR010645>
- O'Haver, T. C. (1991). An introduction to signal processing in chemical measurement. *Journal of Chemical Education*, 68(6), A147. <https://doi.org/10.1021/ed068pA147>
- Okamoto, S. (1982). Turbulent shear flow behind hemisphere-cylinder placed on ground plane. In L. J. S. Bradbury, F. Durst, B. E. Launder, F. W. Schmidt, & J. H. Whitelaw (Eds.), *Turbulent shear flows 3*, (pp. 171–185). Berlin, Germany: Springer. https://doi.org/10.1007/978-3-642-95410-8_17
- Paik, J., Escauriaza, C., & Sotiropoulos, F. (2007). On the bimodal dynamics of the turbulent horseshoe vortex system in a wing-body junction. *Physics of Fluids*, 19(4), 045107. <https://doi.org/10.1063/1.2716813>
- Papanicolaou, A. N. (2012). Aspects of secondary flow in open channels: A critical literature review. In M. Church, P. M. Biron, & A. G. Roy (Eds.), *Gravel-bed rivers: Processes, tools, environments*, (pp. 31–35). Chichester, UK: Wiley-Blackwell. <https://doi.org/10.1002/9781119952497.ch3>
- Papanicolaou, A. N., Dermisis, D. C., & Elhakeem, M. (2011). Investigating the role of clasts on the movement of sand in gravel bed rivers. *Journal of Hydraulic Engineering*, 137(9), 871–883. [https://doi.org/10.1061/\(ASCE\)HY.1943-7900.0000381](https://doi.org/10.1061/(ASCE)HY.1943-7900.0000381)
- Papanicolaou, A. N., Diplas, P., Evangelopoulos, N., & Fotopoulos, S. (2002). Stochastic incipient motion criterion for spheres under various bed packing conditions. *Journal of Hydraulic Engineering*, 128(4), 369–380. [https://doi.org/10.1061/\(ASCE\)0733-9429\(2002\)128:4\(369\)](https://doi.org/10.1061/(ASCE)0733-9429(2002)128:4(369))
- Papanicolaou, A. N., Elhakeem, M., & Knapp, D. D. (2009). Evaluation of a gravel transport sensor for bed load measurements in natural flows. *International Journal of Sediment Research*, 24(1), 1–15. [https://doi.org/10.1016/S1001-6279\(09\)60012-3](https://doi.org/10.1016/S1001-6279(09)60012-3)
- Papanicolaou, A. N., & Knapp, D. D. (2010). A particle tracking technique for bedload motion. *US Geological Survey Scientific Investigations Report*, 5091, 352–366.
- Papanicolaou, A. N., & Kramer, C. M. (2005). The role of relative submergence on cluster microtopography and bedload predictions in mountain streams. In G. Parker, & M. H. Garcia (Eds.), *Proc. 4th Int. Symp "River, coastal and estuarine morphodynamics"*, (pp. 1083–1086). Philadelphia, Urbana, IL: Taylor and Francis.
- Papanicolaou, A. N., Kramer, C. M., Tsakiris, A. G., Stoesser, T., Bomminayi, S., & Chen, Z. (2012). Effects of a fully submerged boulder within a boulder array on the mean and turbulent flow fields: Implications to bedload transport. *Acta Geophysica*, 60(6), 1502–1546. <https://doi.org/10.2478/s11600-012-0044-6>
- Papanicolaou, A. N., & Schuyler, A. (2003). Cluster evolution and flow-frictional characteristics under different sediment availabilities and specific gravity. *Journal of Engineering Mechanics*, 129(10), 1206–1219. [https://doi.org/10.1061/\(ASCE\)0733-9399\(2003\)129:10\(1206\)](https://doi.org/10.1061/(ASCE)0733-9399(2003)129:10(1206))
- Papanicolaou, A. N., & Tsakiris, A. G. (2017). Boulder effects on turbulence and bedload transport. In D. Tsutsumi, & J. B. Laronne (Eds.), *Gravel bed rivers: Processes and disasters*, (pp. 33–72). Hoboken, NJ: Wiley. <https://doi.org/10.1002/978118971437.ch2>
- Pitlick, J. (1994). Relation between peak flows, precipitation, and physiography for five mountainous regions in the western USA. *Journal of Hydrology*, 158(3–4), 219–240. [https://doi.org/10.1016/0022-1694\(94\)90055-8](https://doi.org/10.1016/0022-1694(94)90055-8)
- Pitlick, J., Mueller, E. R., Segura, C., Cress, R., & Torizzo, M. (2008). Relation between flow, surface-layer armoring and sediment transport in gravel-bed rivers. *Earth Surface Processes and Landforms*, 33(8), 1192–1209. <https://doi.org/10.1002/esp.1607>
- Piton, G., & Recking, A. (2015). Design of sediment traps with open check dams. I: Hydraulic and deposition processes. *Journal of Hydraulic Engineering*, 142(2), 04015045. [https://doi.org/10.1061/\(ASCE\)HY.1943-7900.0001048](https://doi.org/10.1061/(ASCE)HY.1943-7900.0001048)
- Recking, A., Frey, P., Paquier, A., & Belleudy, P. (2009). An experimental investigation of mechanisms involved in bed load sheet production and migration. *Journal of Geophysical Research*, 114, F03010. <https://doi.org/10.1029/2008JF000990>
- Rickenmann, D. (2001). Comparison of bed load transport in torrents and gravel bed streams. *Water Resources Research*, 37(12), 3295–3305. <https://doi.org/10.1029/2001WR000319>
- Riviere, N., Vouillat, G., Launay, G., & Mignot, E. (2017). Emerging obstacles in supercritical open-channel flows: Detached hydraulic jump versus wall-jet-like bow wave. *Journal of Hydraulic Engineering*, 143(7), 04017011. [https://doi.org/10.1061/\(ASCE\)HY.1943-7900.0001291](https://doi.org/10.1061/(ASCE)HY.1943-7900.0001291)
- Scheingross, J. S., Winchell, E. W., Lamb, M. P., & Dietrich, W. E. (2013). Influence of bed patchiness, slope, grain hiding, and form drag on gravel mobilization in very steep streams. *Journal of Geophysical Research: Earth Surface*, 118, 982–1001. <https://doi.org/10.1002/jgrf.20067>
- Schmeeckle, M. W., Nelson, J. M., & Shreve, R. L. (2007). Forces on stationary particles in near-bed turbulent flows. *Journal of Geophysical Research*, 112, F02003. <https://doi.org/10.1029/2006JF000536>
- Schneider, J. M., Rickenmann, D., Turowski, J. M., Bunte, K., & Kirchner, J. W. (2015). Applicability of bed load transport models for mixed-size sediments in steep streams considering macro-roughness. *Water Resources Research*, 51, 5260–5283. <https://doi.org/10.1002/2014WR016417>
- Seminara, G., Colombini, M., & Parker, G. (1996). Nearly pure sorting waves and formation of bedload sheets. *Journal of Fluid Mechanics*, 312(1), 253–278. <https://doi.org/10.1017/S0022112096001991>
- Shamloo, H., Rajaratnam, N., & Katopodis, C. (2001). Hydraulics of simple habitat structures. *Journal of Hydraulic Research*, 39(4), 351–366. <https://doi.org/10.1080/00221680109499840>
- Sklar, L. S., Fadde, J., Venditti, J. G., Nelson, P. A., Wydzga, M. A., Cui, Y., & Dietrich, W. E. (2009). Translation and dispersion of sediment pulses in flume experiments simulating gravel augmentation below dams. *Water Resources Research*, 45, W08439. <https://doi.org/10.1029/2008WR007346>

- Steidtmann, J. R. (1982). Size–density sorting of sand-size spheres during deposition from bedload transport and implications concerning hydraulic equivalence. *Sedimentology*, 29(6), 877–883. <https://doi.org/10.1111/j.1365-3091.1982.tb00090.x>
- Strom, K. B., Papanicolaou, A. N., Evangelopoulos, N., & Odeh, M. (2004). Microforms in gravel bed rivers: Formation, disintegration, and effects on bedload transport. *Journal of Hydraulic Engineering*, 130(6), 554–567. [https://doi.org/10.1061/\(ASCE\)0733-9429\(2004\)130:6\(554\)](https://doi.org/10.1061/(ASCE)0733-9429(2004)130:6(554))
- Tamburino, A., & Gulliver, J. S. (1999). Large flow structures in a turbulent open channel flow. *Journal of Hydraulic Research*, 37(3), 363–380. <https://doi.org/10.1080/00221686.1999.9628253>
- Tsakiris, A. G., Papanicolaou, A. N., Hajimírzaie, S. M., & Buchholz, J. H. J. (2014). Influence of collective boulder array on the surrounding time-averaged and turbulent flow fields. *Journal of Mountain Science*, 11(6), 1420–1428. <https://doi.org/10.1007/s11629-014-3055-8>
- Tsakiris, A. G., Papanicolaou, A. N., & Lauth, T. J. (2014). Signature of bedload particle transport mode in the acoustic signal of a geophone. *Journal of Hydraulic Research*, 52(2), 185–204. <https://doi.org/10.1080/00221686.2013.876454>
- Turowski, J. M., Yager, E. M., Badoux, A., Rickenmann, D., & Molnar, P. (2009). The impact of exceptional events on erosion, bedload transport and channel stability in a step-pool channel. *Earth Surface Processes and Landforms*, 34(12), 1661–1673. <https://doi.org/10.1002/esp.1855>
- Uchida, T., Fukuoka, S., Papanicolaou, A. N., & Tsakiris, A. G. (2016). Nonhydrostatic quasi-3D model coupled with the dynamic rough wall law for simulating flow over a rough bed with submerged boulders. *Journal of Hydraulic Engineering*, 142(11), 04016054. [https://doi.org/10.1061/\(ASCE\)HY.1943-7900.0001198](https://doi.org/10.1061/(ASCE)HY.1943-7900.0001198)
- Yager, E. M., Dietrich, W. E., Kirchner, J. W., & Mc Ardell, B. (2012). Patch dynamics and stability in steep, rough streams. *Journal of Geophysical Research*, 117, F02010. <https://doi.org/10.1029/2011JF002253>
- Yager, E. M., Kirchner, J. W., & Dietrich, W. E. (2007). Calculating bed load transport in steep boulder bed channels. *Water Resources Research*, 43, W07418. <https://doi.org/10.1029/2006WR005432>